Author/s:
Ahmerkamp, S;Jalaluddin, FM;Cui, Y;Brumley, DR;Pacherres, CO;Berg, JS;Stocker, R;Kuypers, MMM;Koren, K;Behrendt, L

Title:
Simultaneous visualization of flow fields and oxygen concentrations to unravel transport and metabolic processes in biological systems

Date:
2022-05-23

Citation:
Ahmerkamp, S., Jalaluddin, F. M., Cui, Y., Brumley, D. R., Pacherres, C. O., Berg, J. S., Stocker, R., Kuypers, M. M. M., Koren, K. & Behrendt, L. (2022). Simultaneous visualization of flow fields and oxygen concentrations to unravel transport and metabolic processes in biological systems. Cell Reports Methods, 2 (5), https://doi.org/10.1016/j.crmeth.2022.100216.

Persistent Link:
https://hdl.handle.net/11343/316150

Cell Reports
Methods

Article

Simultaneous visualization of flow fields and oxygen concentrations to unravel transport and metabolic processes in biological systems

Graphical abstract

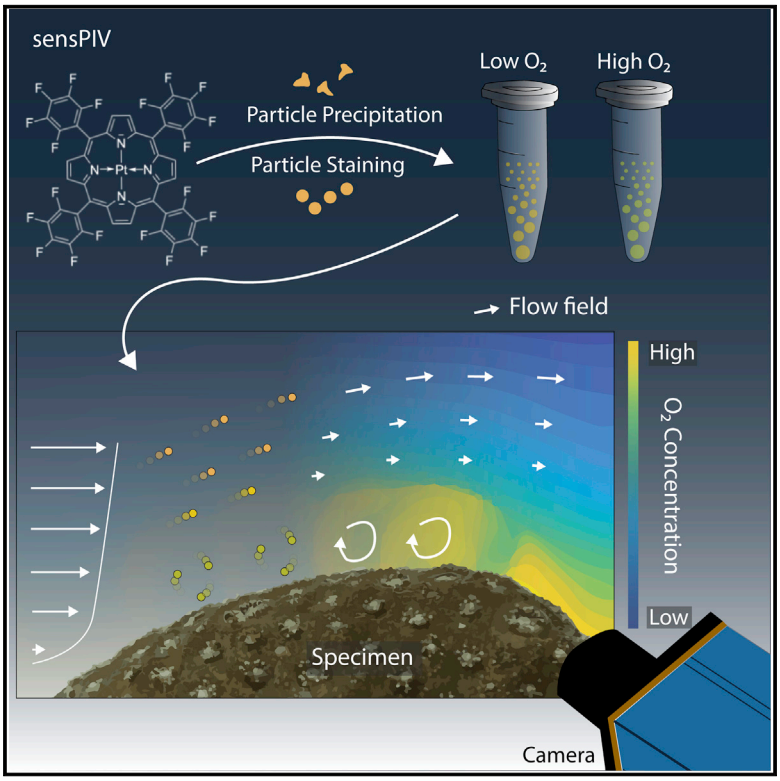

Authors

Soeren Ahmerkamp, Farooq Moin Jalaluddin, Yuan Cui, ..., Marcel M.M. Kuypers, Klaus Koren, Lars Behrendt

Correspondence

sahmerka@mpi-bremen.de (S.A.), klaus.koren@bio.au.dk (K.K.), lars.behrendt@scilifelab.uu.se (L.B.)

In brief

Ahmerkamp et al. present sensPIV, a simple and inexpensive yet powerful method that uses chemically sensing microparticles to quantitatively link oxygen distributions to physical transport processes. SensPIV can be used to study flow-organism interactions across many life-science and engineering applications.

Highlights

- SensPIV uses chemically sensing particles to visualize O_2 concentrations and flows
- Measurements can be performed with simple setups available in many labs
- O_2 transport can be measured in microfluidic devices, aggregates, and live corals
- SensPIV shows that ciliary flows optimize coral metabolism

Ahmerkamp et al., 2022, Cell Reports Methods 2, 100216
May 23, 2022
https://doi.org/10.1016/j.crmeth.2022.100216

CellPress

Cell Reports Methods

CellPress
OPEN ACCESS

Article

Simultaneous visualization of flow fields and oxygen concentrations to unravel transport and metabolic processes in biological systems

Soeren Ahmerkamp,[1,9,10,*] Farooq Moin Jalaluddin,[1,9] Yuan Cui,[2,9] Douglas R. Brumley,[3] Cesar O. Pacherres,[4,8] Jasmine S. Berg,[5] Roman Stocker,[6] Marcel M.M. Kuypers,[1] Klaus Koren,[7,*] and Lars Behrendt[2,*]

[1]Max Planck Institute for Marine Microbiology, 28359 Bremen, Germany
[2]Science for Life Laboratory, Department of Organismal Biology, Uppsala University, Norbyvägen 18A, SE-752 36 Uppsala, Sweden
[3]School of Mathematics and Statistics, The University of Melbourne, Parkville, VIC 3010, Australia
[4]Alfred Wegener Institute, Helmholtz Centre for Polar and Marine Research, Bremerhaven, Germany
[5]Institute of Earth Surface Dynamics, University of Lausanne, 1015 Lausanne, Switzerland
[6]Institute for Environmental Engineering, Department of Civil, Environmental and Geomatic Engineering, ETH Zurich, 8093 Zurich, Switzerland
[7]Aarhus University Centre for Water Technology, Department of Biology, Aarhus University, 8000 Aarhus, Denmark
[8]Present address: Department of Biology, Copenhagen University, Copenhagen, Denmark
[9]These authors contributed equally
[10]Lead contact
*Correspondence: sahmerka@mpi-bremen.de (S.A.), klaus.koren@bio.au.dk (K.K.), lars.behrendt@scilifelab.uu.se (L.B.)
https://doi.org/10.1016/j.crmeth.2022.100216

MOTIVATION In aquatic environments, oxygen (O_2) production and consumption are intimately connected via transport processes. Many organisms interact with or generate flow fields to enhance exchange processes and optimize their metabolism, yet our understanding on these complex interactions is mostly derived from simplified mathematical models. This is primarily because we lack methods that can accurately measure transport processes and O_2 concentrations at the same time. To address this problem, we developed "sensPIV," a simple and inexpensive yet powerful method that uses chemically sensing microparticles to quantitatively link O_2 distributions to physical transport processes.

SUMMARY

From individual cells to whole organisms, O_2 transport unfolds across micrometer- to millimeter-length scales and can change within milliseconds in response to fluid flows and organismal behavior. The spatiotemporal complexity of these processes makes the accurate assessment of O_2 dynamics via currently available methods difficult or unreliable. Here, we present "sensPIV," a method to simultaneously measure O_2 concentrations and flow fields. By tracking O_2-sensitive microparticles in flow using imaging technologies that allow for instantaneous referencing, we measured O_2 transport within (1) microfluidic devices, (2) sinking model aggregates, and (3) complex colony-forming corals. Through the use of sensPIV, we find that corals use ciliary movement to link zones of photosynthetic O_2 production to zones of O_2 consumption. SensPIV can potentially be extendable to study flow-organism interactions across many life-science and engineering applications.

INTRODUCTION

The production of dioxygen (O_2) by photosynthesis began approximately 2.3 bya, and the high energy yield obtained from O_2 respiration enabled the development of multicellular life on Earth (Falkowski, 2006; Bekker et al., 2004). However, the poor water solubility of O_2 places fundamental constraints on biological metabolism. The molecular diffusion of O_2, or diffusive flux, around and into cells is typically slow compared with intracellular reaction rates. To expedite the transport of O_2 from regions of production to consumption, life has evolved a range of ventilation mechanisms to enhance fluid flow in close proximity of cells. The magnitude and direction of this flow transports solutes, resulting in an advective flux. In systems ranging from coral surfaces to circulatory systems of animals, biological metabolism and physical transport processes (i.e., advection and diffusion) are intimately linked and unfold dynamically (from milliseconds to days) across spatial scales (micrometer to millimeter). Charting the complex interplay between O_2 production, consumption, and transport processes is only possible through simultaneously measuring these quantities in a dynamic fashion. However, existing methods have largely focused on

measuring O_2 concentrations and transport processes separately. Here, we expand the toolbox of existing O_2-sensing techniques by combining particle image velocimetry (PIV) with optode-based chemical sensing. This method, chemical-sensing PIV ("sensPIV"), now enables measurements of transport processes and O_2 concentrations simultaneously across spatial scales and environments.

Microscale transport is usually measured on particle ensembles via PIV or by particle-tracking velocimetry (PTV), which tracks individual particles in fluid flow. Both methods repeatedly image naturally occurring or artificially added particles (typical size 0.1–10 μm) to obtain information about the local speed and direction of fluid flow. Based on this information, flow fields can be accurately reconstructed in 2D or using stereoscopic or tomographic approaches in 3D (Raffel et al., 1998; Westerweel et al., 2013). A number of commercially available PIV systems and image-processing tools have enabled researchers to describe transport processes, such as blood flow through cardiovascular systems (Yousif et al., 2011; Kheradvar et al., 2010), or the interaction of small crustacea (Gemmell et al., 2014), flocs or particles (Zetsche et al., 2020), jellyfish (Costello et al., 2021; Gemmell et al., 2015), and planktonic protists (Drescher et al., 2010; Nielsen and Kiørboe, 2021; Gilpin et al., 2017) with their flow field. While these studies have provided insights into the interaction of organisms with surrounding flow fields during propulsion or foraging, they do not provide a quantitative assessment of how transport processes affect fluxes of O_2.

Microscale O_2 measurements have traditionally been performed using amperometric micro-electrodes (Clark et al., 1953). Owing to their high accuracy and resolution, microsensors have decisively influenced our understanding of the role of O_2 in biogeochemical processes (Revsbech and Jørgensen, 1986), human physiology (Sheffield, 1998), and plant physiology (Pedersen et al., 1998). More recently, optical sensors called optodes have emerged as powerful tools for measuring O_2. This technology is based on the O_2-dependent phosphorescence quenching of a chemical indicator enabling contactless O_2 sensing (Morris et al., 1993; Klimant et al., 1995). By entrapping the indicator chemical in a polymeric matrix, surfaces can be coated, resulting in a variety of sensor types, such as optical fibers or planar optodes. Planar optodes enable the imaging of O_2 in 2D and have revolutionized our understanding of O_2 distributions and their heterogeneity within complex biological samples, like sediments (Frederiksen and Glud, 2006; Stockdale et al., 2009; Meysman et al., 2010), corals (Holst et al., 2002) or dental plaque (Khosravi et al., 2020). Recently, micro- and nanoparticle-based optodes (optode particles) have been used to visualize O_2 concentrations around micro-organisms (Kühl et al., 2020), within micro-organisms (Okkelman et al., 2020; Zhdanov et al., 2015; Tobita and Yoshihara, 2016), and in the bone marrow of live animals (Spencer et al., 2014). Despite these powerful applications, the drawbacks of optodes include their low temporal resolution and the fact that planar optodes affect advective transport by acting as a wall and modifying the flow. As a result, optodes are typically applied to static measurements of O_2 concentrations and diffusive transport. In nature, however, organisms interact with complex O_2 gradients emanating from changing flow, aerotaxis, or O_2 uptake (Stocker, 2012; Guasto et al., 2012). Studying the microscale organization of O_2 fluxes thus requires the ability to concurrently visualize O_2 gradients and advective transport.

The importance of combining measurements of transport processes and O_2 concentrations has already been highlighted by some studies. For example, sequential measurements using PIV and microsensors uncovered the effects of ciliary flow on O_2 exchange in coral boundary layers (Pacherres et al., 2020; Shapiro et al., 2014). Unfortunately, such studies could not fully resolve the spatial distribution of O_2, as microsensors can disturb flow fields. Concentration gradients and flow within, e.g., the phycosphere of individual algae (Kanso et al., 2021) or suspensions of micro-organisms (Sommer et al., 2017) may also exhibit strong variation in time and space, and to measure such minute changes in O_2, it is important to apply sensors that are non-invasive. Yet only a handful of studies (Kim et al., 2013; Abe et al., 2004) have succeeded in measuring O_2 concentrations and advective flow simultaneously and non-invasively using complex, highly controlled experimental setups. In particular, difficulties in compensating for uneven illumination and small windows of detectable O_2 concentrations have prevented a broad implementation of these techniques. A simple, reliable, and reproducible approach that combines measurements of transport processes with O_2-sensing is needed to enable the systematic study of how organisms interact with and modify their environment to optimize transport across a range of spatial scales.

Here, we present sensPIV, a method that combines the ability of optodes to dynamically measure O_2 with the ability of PIV to accurately resolve advective and diffusive transport processes. Using sensPIV, the interplay between transport processes and biological reactions can now be investigated at high resolution across a range of environments using experimental setups available in many laboratories. We demonstrate the versatility of sensPIV by applying it to three contrasting experimental systems of increasing complexity: microfluidic devices, artificial marine aggregates, and living coral fragments. Our sensPIV measurements reveal how flow fields increase exchange processes around particles and how corals actively modulate their microenvironment to enhance the flux of O_2.

RESULTS

Method development

There are three essential steps to successfully employ sensPIV: (1) the synthesis of O_2-sensitive optode particles, (2) the correct illumination of optode particles, and (3) the correct choice of imaging modalities.

Synthesis of sensPIV particles

Particles used for sensPIV must exhibit a quantifiable quenching response over a range of O_2 concentrations, fast response times, and good imaging capabilities. Although many O_2-sensitive compounds fulfill these requirements (see, for example, Quaranta et al., 2012 and Wang and Wolfbeis, 2014 for chemistry overview), we recommend the use of platinum(II) meso- (2,3,4,5,6-pentafluoro)phenyl porphyrin (PtTFPP), as it is commercially available, photostable, relatively unaffected by temperature, and exhibits a good sensitivity across a broad range of O_2 concentrations (Figures 1A–1H; Video S1; see Borisov et al., 2008). The dynamic

CellPress
OPEN ACCESS

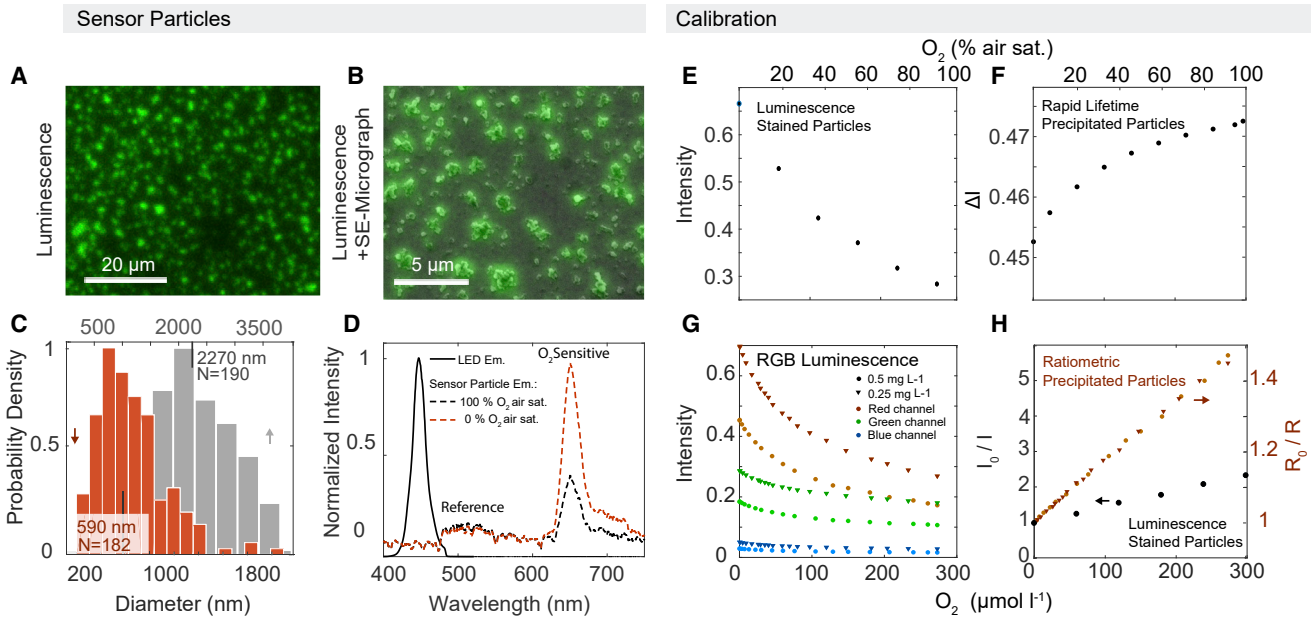

Figure 1. Characterization of the sensor particles

(A) O_2-sensitive sensor particles excited by blue wavelengths (365–440 nm) emit green and red fluorescence (500–650 nm).

(B) Scanning electron micrographs of the same sensor particles as in (A) overlaid with the fluorescent signal.

(C) Size spectrum analysis reveals that sensor particle sizes range between 200 and 1,800 nm (median = 590 nm) for precipitated particles (orange) and 500–4,000 nm (median = 2,270 nm) for stained particles (gray).

(D) Emission spectra of O_2-sensitive sensor particles. Dashed lines indicate the emission of the sensor particles at 0% O_2 air sat. (red) and 100% O_2 air sat. (black). The solid black line indicates the emission spectrum of the LED used for excitation of sensor particles.

(E) The luminescence intensity of stained particles based on the intensity of the camera pixel.

(F) Rapid lifetime measurement of precipitated particles as a function of O_2 concentrations.

(G) Luminescence imaging of precipitated ratiometric sensPIV particles with an RGB camera. Note that, as a result of the spectral overlap between channels, the green channel also exhibits a slight O_2 dependency. The concentrations of 0.5 mg L^{-1} (red, triangles) and 0.25 mg L^{-1} (orange, round) refer to the tested sensor particle concentrations.

(H) Calibration curve for two types of sensor particles at different concentrations of O_2. Orange and red colors denote particles produced via precipitation (0.5 mg L^{-1}: red triangles; 0.25 mg L^{-1}: orange circles), and black colors denote particles produced via staining methods.

quenching of PtTFPP by O_2 leads to a reversible, O_2-dependent change in luminescence intensity as well as luminescence lifetime. This relationship is described by the Stern-Volmer relationship,

$$\frac{\tau_0}{\tau} - 1 = \frac{I_0}{I} - 1 = K_{SV} \cdot [O_2], \qquad \text{(Equation 1)}$$

where K_{sv} is the Stern-Volmer constant, $[O_2]$ is the dissolved O_2 concentration, I is the luminescence intensity at a given dissolved O_2 concentration, and I_0 is the luminescence intensity in the absence of O_2. The same relationship applies to the luminescence lifetime in the presence (τ) and absence of O_2 (τ_0). From Equation 1, consequently, the calibration of sensPIV particles can be performed by measuring the luminescence intensities of O_2-sensitive dyes at known O_2 concentrations.

To synthesize suitable particles for sensPIV, we explored two methods: (1) a precipitation method (Mistlberger et al., 2010) and (2) a staining method that uses commercially available particles (diameter of 2.3 µm; Figures 1A–1D and S1A). Precipitation is a straightforward process where an indicator dye (PtTFPP), a reference dye (Macrolex fluorescence yellow 10GN), and a polymer (styrene maleic anhydride) are dissolved in a solvent (tetrahydrofuran) that is well miscible with water (see STAR Methods). As dyes and the polymer are water insoluble, precipitation of dye-containing particles (size 200–1,800 nm) occurs instantaneously when mixed with water (Figures 1A–1C and S1A). To prevent particle aggregation, we used a copolymer of styrene and maleic anhydride. During precipitation, the anhydride groups are hydrolyzed and the resulting carbonic acid groups on the surface stabilize the particles (see Mistlberger et al., 2010 for tuning possibilities of nanoparticles). The main advantage of precipitation is the possibility of producing large amounts of sensor particles with minimal effort and virtually no specialized equipment. In contrast to precipitation, the staining method uses commercially available synthetic particles that are exposed to a mixture of an organic solvent (here acetone) and water with added O_2 indicator PtTFPP (Borisov et al., 2008). Particles immersed in this mixture swell and entrap lipophilic dyes within the particles when the organic solvent evaporates.

Notably, both synthesis methods produce particles that contain a range of different particle sizes (Figure 1C; 590 ± 360 nm [SD] by precipitation and 2,270 ± 1960 nm by staining) and, in order to suppress variability in particle sizes, we developed a protocol consisting of a series of sonication, centrifugation, and subsequent

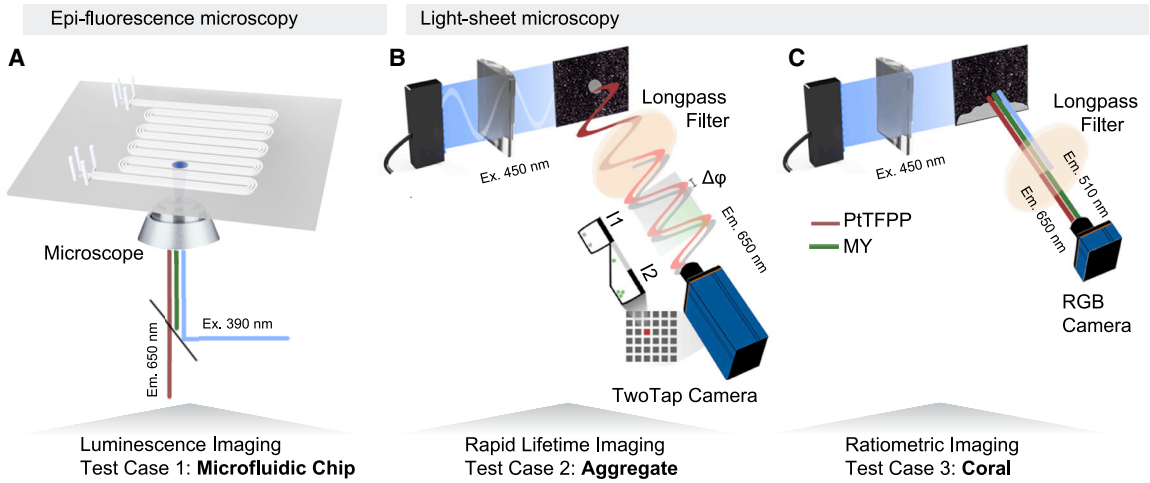

Figure 2. Conceptual illustration of the three imaging approaches compatible with sensPIV and used within this study

(A) Luminescence intensity imaging: here, UV light (~390 nm) is used to excite the O_2-sensitive dye (PtTFPP) on sensPIV particles. The resulting red-shifted (>650 nm) luminescence intensity depends on ambient O_2 concentrations. This approach is achievable using a simple epifluorescence microscope.

(B) Rapid lifetime imaging: here, sensPIV particles are excited with an intensity-modulated light sheet (~450 nm) and the luminescence (~650 nm) emitted by sensor particles is phase shifted. The resulting phase shift $\Delta\varphi$ depends on the O_2 concentration and is estimated based on a two-tap camera chip (see STAR Methods).

(C) Ratiometric imaging: here, blue light (~450 nm) is used to excite both PtTFPP (via energy transfer; see text) and the reference dye, MY. The emission of the PtTFPP (red, R; ~650 nm) is normalized by the emission of MY (green, G; ~500 nm), which compensates for inhomogeneous illumination and simplifies calibration.

filtration steps (described in STAR Methods and Figure S1B). We found that, despite inhomogeneous particle sizes, a simple two-point calibration is sufficient for accurate O_2 measurements via sensPIV (Figures 1E–1H).

Excitation and imaging of sensPIV particles

Quantifying the O_2-dependent phosphorescence (Morris et al., 1993; Klimant et al., 1995) of nano- and micrometer-sized sensPIV particles requires microscale visualization. In this study, we examined sensPIV particles via epifluorescence microscopy or light-sheet microscopy (Figures 2A–2C). Standard epifluorescence microscopes can be readily adapted for sensPIV measurements, either by using existing laser- or diode-based light sources to excite PtTFPP (excitation [Ex.] ≈ 390 nm) or by adding a specific fluorescence filter cube (e.g., Ex. ≈ 390 nm; emission [Em.] > 490 nm) when using full-spectrum light sources (Figures 2A–2C). Epifluorescence microscopes are available in many research environments and are well suited to perform sensPIV in well-defined experimental setups (e.g., microfluidic applications). Compared with epifluorescence microscopy, light-sheet microscopy can be used to image sensPIV particles around larger 3D objects (mm-cm scale) or in experimental setups that require additional instrumentation, such as flow chambers. Light-sheet microscopy, however, requires high light intensities and a homogeneous illumination field, which is achievable only with high-power light-emitting diode (LED) systems with an output ranging between 2.5 W and 5 W or with laser diodes (see STAR Methods section).

Simultaneously recording fluid movement and local O_2 concentration via sensPIV particles requires fast cameras (>10 Hz for the applied test cases) in order to capture the luminescence of rapidly moving particles. Capturing differences in luminescence is achieved via three imaging modalities, (1) luminescence imaging (Figure 2A), (2) ratiometric imaging (Figure 2B), and (3) rapid lifetime imaging (Figure 2C). In its simplest form, sensPIV can be executed by recording the luminescence intensity of sensor particles with a simple monochromatic camera. Such cameras are characterized by high quantum efficiencies, which allow for lower excitation intensities and faster recording frequencies (>100 Hz). However, the accuracy of measurements with monochromatic cameras is usually limited by the homogeneity of the illumination, which may be affected through shading when observed samples exhibit three-dimensionality. In our proof-of-concept applications, we demonstrate that effects of inhomogeneous excitation light can be avoided by performing *in situ* calibrations of sensor particles in simplified, controlled environments (such as microfluidic devices; see test case 1) or by using alternative imaging methods (such as ratiometric or rapid lifetime imaging) that record the light used for excitation at the same time as the emission light, thereby enabling instantaneous referencing.

Ratiometric imaging takes advantage of two luminescent dyes present within the same sensPIV particle to obtain a ratio of luminescence signals. One dye serves as the O_2-sensitive indicator, while the second O_2-insensitive dye acts as a reference. Normalizing the intensity of the O_2-sensitive dye with the reference intensity compensates for inhomogeneous illumination fields, particle sizes, and artifacts introduced by topographic features (see Koren et al., 2015 and references therein). Ideally, ratiometric dyes cover two colors of the RGB chip installed in many commercially available cameras, which allows for convenient sensPIV measurements by taking a single image. In our experiments, we optimized the synthesis of PtTFPP sensor particles

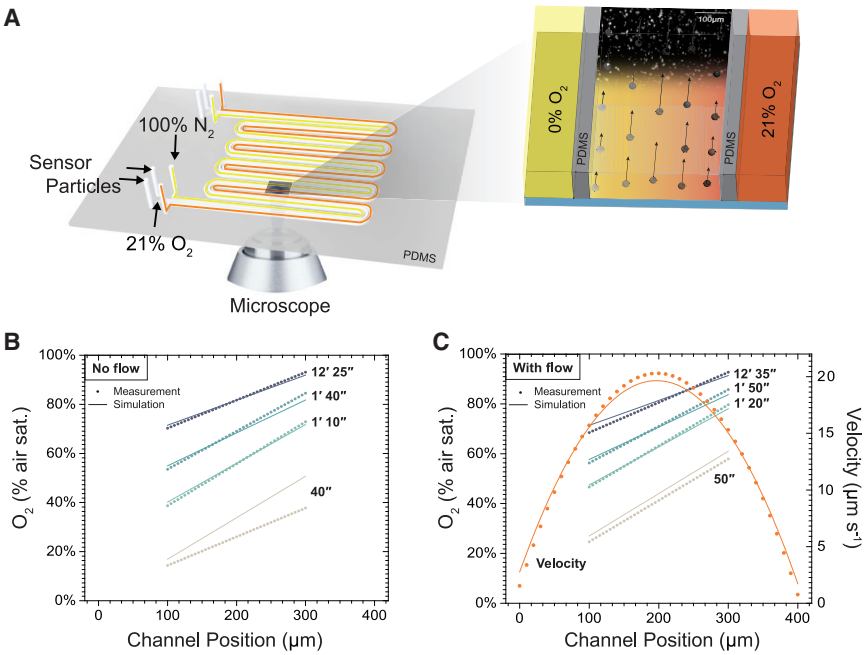

Figure 3. The behavior of sensPIV particles in a simple microfluidic device with a well-defined linear O_2 profile

(A) Cross-section of the microfluidic device used to control the gas environment around sensPIV particles. The microfluidic device was adapted from Rusconi et al., 2014b) and consists of a central fluidic channel surrounded by two (gas) side channels. Injecting 100% N_2 (0% O_2) into one of the gas channels and compressed air (21% O_2) into the other resulted in a linear O_2 gradient across the central fluidic channel containing sensPIV particles.

(B) O_2 profiles in no flow conditions. Here, sensPIV particles were introduced into the main channel and kept quiescent. Shown are sensPIV measurements (dotted lines) and model simulations (solid lines) at time 40 s, 1 min 10 s, 1 min 40 s, and 12 min 25 s.

(C) O_2 profiles under flow conditions. Here, sensPIV particles were continuously introduced into the main fluidic channel at a flow velocity of 11 $\mu m\ s^{-1}$. Comparison between sensPIV measurements and model simulations at 50 s, 1 min 20 s, 1 min 50 s, and 12 min 35 s is shown (correlation coefficients are presented in Table S1).

for ratiometric sensPIV (see above and supplemental information; test case 3 for application). The O_2-sensitive compound PtTFPP (Em. peak at ~650 nm) in combination with the reference dye Macrolex fluorescent yellow 10GN (MY) (Em. peak at ~480 nm) yields optimal performance in combination with standard RGB cameras (see also Koren et al., 2015). Notably, MY does not only act as a reference dye but also acts as an antenna molecule that transfers excitation energy to PtTFPP and thereby increases sensor brightness via light-harvesting effects (see Mayr et al., 2009). Instead of less powerful green or potentially harmful UV LEDs, which target the specific absorbance spectra of PtTFPP, it is therefore possible to work with less harmful and bright-blue LEDs.

To measure dissolved O_2 concentrations without addition of a reference dye, luminescent lifetime imaging is the method of choice (Holst et al., 2002; Murniati et al., 2016). The luminescence lifetime is the mean time between activation of a molecule and photon emission and is characteristic for every luminophore. The lifetime of the O_2-sensitive PtTFPP (~60 µs without O_2) can be estimated via repeated imaging of the declining luminescence intensity after light exposure (see Koren et al., 2019). However, for typical shutter-modulated cameras, readout times are on the order of 10–100 s due to relatively slow sensors. Newer cameras allow for estimating the lifetime (τ) in the frequency domain based on the frequency shift (see key resources table and STAR Methods) and can capture lifetime images in less than 10 s (Koren et al., 2019). In order to meet the requirements for sensPIV (recording frequencies >10 Hz), we performed rapid lifetime measurements with a camera chip (QMFLIM2, pco) that has an in-pixel charge swing separating two taps within each pixel (Chen et al., 2015). The in-pixel charge swing allows quasi-instantaneous recording of two sequential images (I_{T1} and I_{T2}), where each image covers half the period of the excitation signal (5 kHz; see Figure 2). The normalized intensity difference of the two images $\Delta I = (I_{T1} - I_{T2})/(I_{T1} + I_{T2})$ is directly related to the dissolved O_2 concentration (see Figure 2C). The advantage of lifetime imaging is that only one O_2-sensitive dye is needed and highly accurate measurements are achievable, even in heterogeneous samples (see test case 2 for application). The main disadvantages of this method are (1) the relatively high cost of the camera system and (2) that measured signals do not scale linearly (Figure 1F), which requires the application of a second-order polynomial fit (see STAR Methods).

Applications of sensPIVv

SensPIV under well-defined O_2 gradients within microfluidic devices

Microfluidic chambers are ideal testing arenas for sensPIV, as they provide a high level of control over fluid flows, O_2 concentrations, and imaging of microscale processes (Son et al., 2015). Owing to the importance of viscosity at small scales, fluid flows in microfluidic channels are laminar and exact mathematical solutions allow for robust calibration of flow measurements in prototypical channel geometries, like rectangular channels (Batchelor, 2000). Moreover, specific O_2 concentrations can be controlled and varied over time (Garren et al., 2014; Rusconi et al., 2014a, 2014b; Yawata et al., 2014). These characteristics make microfluidic devices useful for biological and medical applications, including the study of bacterial aerotaxis and measuring O_2-dependent cellular responses (Menolascina et al., 2017). Here, we used microfluidic devices to carefully calibrate sensPIV particles and to demonstrate accurate, simultaneous visualization of fluid flows and O_2 concentrations.

First, we introduced sensPIV particles into a polydimethylsiloxane (PDMS) microfluidic device consisting of a main fluid channel surrounded by two adjacent gas channels (Figure 3A). As PDMS is gas permeable, we can control dissolved O_2 concentrations in the main fluid channel containing sensPIV particles. To calibrate

sensPIV particles, we equilibrated the fluid in the main channel first with compressed air (21% O_2) and then with nitrogen gas (0% O_2) while measuring the luminescence intensity of particles under no flow. Following this two-point calibration, we supplied compressed air to one of the gas channels and nitrogen gas to the other, ultimately resulting in a steady linear O_2 gradient across the main channel. By relating the luminescence intensity of individual sensPIV particles to a previously obtained calibration curve, we could observe the evolution of O_2 concentrations across the main channel (Figure 3B), as the system transitioned to the steady linear profile. This allowed us to compare our experimental O_2 measurements with a time-resolved numerical model solving the scalar transport equations (Figure 3B; see STAR Methods section). This revealed that experimental O_2 concentrations reached equilibrium after 70–100 s, which is consistent with diffusion timescales derived from our model. Experimental data and model results were in good agreement and demonstrated correlation coefficients (R) between 0.75 and 0.82 (Figure 3B; 1 indicating good positive correlation; Table S1). Dissimilarities between model results and experimental results occurred during the initialization of experiments, an observation we attribute to the capacity of PDMS to retain gases and the difference in the time required for gases to be released. Together, these experiments demonstrate that stationary sensPIV particles can visualize steady-state and dynamically changing O_2 concentrations in simple microfluidic geometries.

Second, to determine whether sensPIV particles can accurately visualize transport processes and O_2 concentrations simultaneously, we used the same microfluidic device to control both O_2 concentrations and particle velocities in the main channel. At an average flow speed of 11 $\mu m\ s^{-1}$ in the fluid channel and a compressed gas supply of 21% O_2 and 0% O_2 to the gas channels, we tracked and measured the intensity of sensPIV particles to simultaneously determine flow fields and local O_2 concentrations (Figure 3C). This enabled us to derive the characteristic flow field in the main channel (a parabolic shape) and concurrently visualize the developing gradients of O_2. Experimental data on flow fields and local O_2 concentrations largely matched numerical modeling outputs (Figure 3C; $R_{velocity} = 0.83$; $R_{gradient} = 0.79–0.84$; Table S1) and demonstrated that the equilibrium profile was attained after approximately 80–110 s.

SensPIV for measuring the dynamic O_2 exchange around a model laboratory aggregate

Sedimentation of particles, flocs, or aggregates is a process occurring in both natural and industrial settings, including particulate matter transport in the ocean and deposition in wastewater treatment plants. In organic aggregates, the high carbon content and associated microbial activity lead to the formation of distinct microenvironments. When respiration exhausts O_2 inside aggregates (Ploug, 2001), anaerobic processes are favored (e.g., denitrification and anammox), resulting in the enhanced removal of nutrients in wastewater treatment plants (Speth et al., 2016) and the ocean (Bianchi et al., 2018; Karthäuser et al., 2021). Inside aggregates, the duration and extent of O_2 depletion is governed by the external supply of O_2 and its transport through the aggregate boundary layer. The thickness of the aggregate boundary layer controls O_2 fluxes into aggregates and is highly dependent on the surrounding flow field. Here, we used sensPIV to quantitatively assess the O_2 exchange processes around and into millimeter-sized aggregates. For this, we synthesized porous agarose aggregates (porosity, i.e., the ratio of voids to total volume, $\theta = 0.97 \pm 0.01$; radius, $r = 2.7 \pm 0.1$ mm; n = 6) with embedded sensor particles (produced via the precipitation method). To simulate an O_2-depleted, sinking aggregate, agarose aggregates were degassed and placed into a temperature-compensated flow chamber (Figure 4A). Two separate experiments were performed in which the aggregate was exposed to a flow of 2.1 mm s^{-1}, representing a Reynolds number of approximately 1, and a reference experiment with no flow.

In both experiments, the O_2 boundary layer surrounding the aggregate and the O_2 concentration inside the aggregate were visualized by taking a total of 100 images via rapid lifetime imaging (frequency of 10 Hz; Figure 4B). Flow fields were reconstructed by PTV (Figure S2), and O_2 concentrations were estimated by relating the difference of two intensity images to a calibration curve (Figure 1F; see also Figure S3). High-resolution sensPIV images revealed a 2.5-mm-thick O_2 boundary layer surrounding the aggregate and O_2 concentrations that rapidly decrease from 100% to 90% air saturation in the vicinity of the aggregate surface. The shape of the O_2 boundary layer is narrow on the upstream side and then asymmetrically increases in size toward the downstream side, together confirming previous microsensor-based measurements (Ploug, 2001). We note that, while microsensors provide comparable information, sensPIV measures O_2 transport processes in two dimensions without disturbing flow fields (see also Figure S4).

We next examined the impact of flow on the transfer of O_2 from the aggregate exterior into its interior. To better understand this process, we estimated the diffusion timescale of O_2 into the aggregate ($\tau_D = a^2\ D^{-1} = 32$ min), which qualitatively matched our experimental results with sensPIV (30 min). However, the direct comparison of flow (velocity of 2.1 mm s^{-1}) with no-flow conditions revealed more than 8 % O_2 difference inside the aggregate (measured after 10 min) indicating an enhanced diffusion of O_2. To quantify this enhancement effect, we evaluated the O_2 fluxes, J, through the exterior of the aggregate by calculating the concentration gradient perpendicular to the surface under flow and no-flow conditions. To account for the asymmetry of O_2 concentrations induced by flow fields, all O_2 gradients were averaged along the whole surface of the aggregate following

$$J = -\frac{\theta D}{A}\int \vec{n}\cdot\nabla C\ dA\ ,$$

where D is the diffusion coefficient of O_2, θ is the porosity of the aggregate, and $\vec{n}$ is the unit normal vector perpendicular to the surface of the aggregate (A) resulting in a surface O_2 concentration gradient $\vec{n}\cdot\nabla C$.

After initiating flow, the fluxes of O_2 into the anoxic aggregate core were between 1.3 and 1.8 nmol $cm^{-2}\ s^{-1}$ and declined over time as the aggregate saturated with O_2 (compare Figure 4C). We extracted the fluxes for a given O_2 concentration inside the aggregate and expressed the flow-dependent uptake enhancement as the Sherwood number, which is the ratio of the flux in the presence of flow to the flux in the absence of flow. For the aggregate case, we found an average Sherwood number of 1.75, implying that the fluid flow increased O_2 exchange by 75%

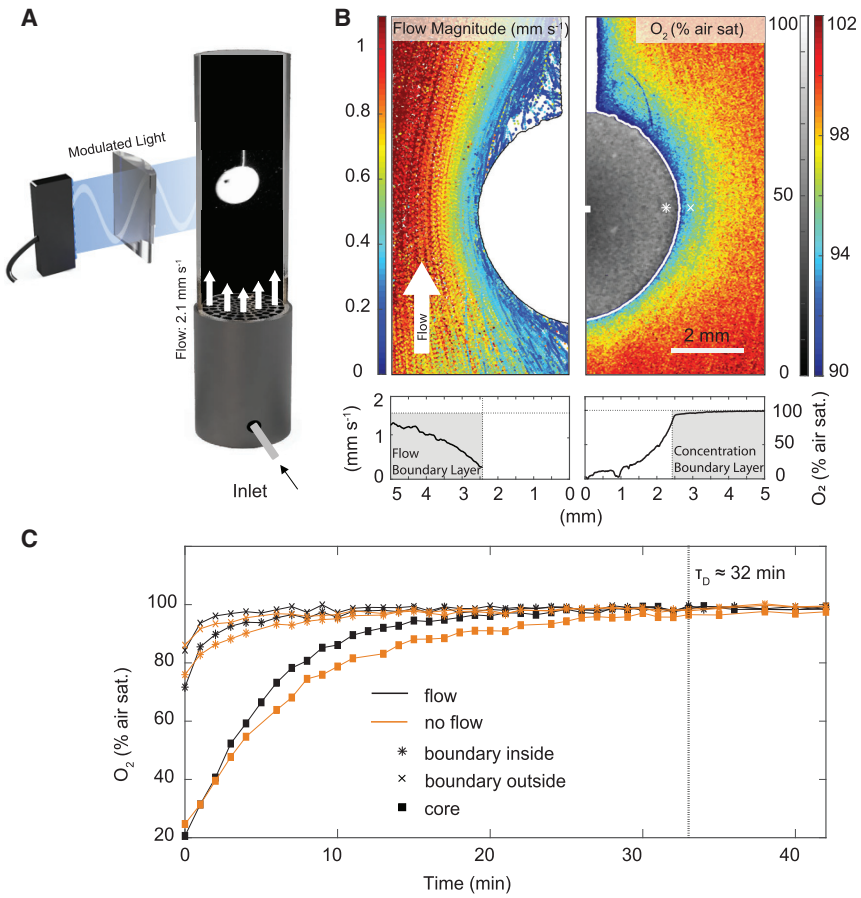

Figure 4. sensPIV visualizes flow and O_2 gradients around and inside a porous agarose aggregate

(A) Conceptual illustration of the experimental setup consisting of a flow chamber, an agarose sphere with embedded sensor particles, and the imaging setup.

(B) Reconstruction of the flow field (left panel) and O_2 concentration inside and around the aggregate (right panel). Note the different scale bars for the O_2 concentration inside and outside the aggregate (see also text). Lower panels indicate flow and O_2 profile along the equator of the aggregate.

(C) Transient O_2 concentrations in the core, at the surface, and in the boundary layer of an aggregate under flow and no-flow conditions. Diffusion timescale τ_D is estimated from the radius of the aggregate and the diffusion of O_2 (see text).

compared with no-flow conditions. This number only represents a single test case and strongly depends on the ratio of settling velocity timescales and diffusion timescales. Previous modeling studies have estimated the uptake enhancement to be about ten times greater for the same spherical aggregate shape and flow regime (Kiørboe and Thygesen, 2001). We attribute this difference to the fact that most models do not take into account aggregate porosity and apply simplified boundary conditions (Moradi et al., 2018). Our visualization of aggregate-fluid exchange processes under flow conditions thus demonstrates the importance of experimentally verifying numerical models. SensPIV is suited to address this challenge and to elucidate how the presence of flow and metabolic activity shapes O_2 gradients.

SensPIV for the visualization of O_2 dynamics and cilia-induced flows around the coral Porites lutea

Cilia are hair-like structures present in many motile micro-organisms but also humans and other mammals (Sleigh, 1962; Wan, 2018). A key function of (motile) cilia is to initiate fluid motion to propel organisms or to enhance ventilation across surfaces (Gilpin et al., 2020). In a final experiment, sensPIV was used to investigate the microscale interaction of epidermal cilia on a reef-building coral with its surrounding flow environment. Previous studies on coral flow fields demonstrated that the beating of epidermal cilia stirs the boundary layer and enhances mass transport (Shapiro et al., 2014). However, due to methodological limitations, it was not fully understood how the flow field generated by cilia affects the O_2 concentrations within the coral boundary layer and what benefit the coral derives from this.

Here, we used the stony coral *Porites lutea* as a model organism and measured sensPIV particles around its surface through a recently developed light-sheet microscope and recirculating flow chamber (Pacherres et al., 2020). First, we tested the biocompatibility of sensPIV particles by adding particles and observing coral cilia beating for 5 min during stroboscopic light exposures (20 ms each). The introduction of sensPIV did not visibly induce coral bleaching or change the beating of cilia but induced substantial mucus production as previously observed under light stress (Fabricius-Dyg et al., 2012; Koren et al., 2016). After experiments, coral fragments were visually inspected for several days and no substantial release of Symbiodiniaceae was detected. Finally, we tested the effects of continuous illumination by exposing a coral fragment to light for 2 min, a duration that is 60 times longer than the total illumination time used in experiments. Prolonged light exposure caused the release of endosymbionts and bleaching of the coral fragments exposed to light. These experiments suggest that sensPIV particles are biocompatible as long as light and particle exposure are minimized. In all subsequent experiments, this was achieved by using short light strobes ($\lesssim$20 ms) and removing sensor particles after finishing experiments ($\sim$1 min).

To visualize O_2 concentrations around *P. lutea*, we introduced sensPIV particles and recorded 100 color images within a time window of 2 s (see also Video S2). Based on these images, we reconstructed the O_2 concentration using a ratiometric-referencing approach with the red (R) and green (G) channels of the color image (Figures 5A and 5B). We found that single images can reconstruct O_2 concentrations with an error of

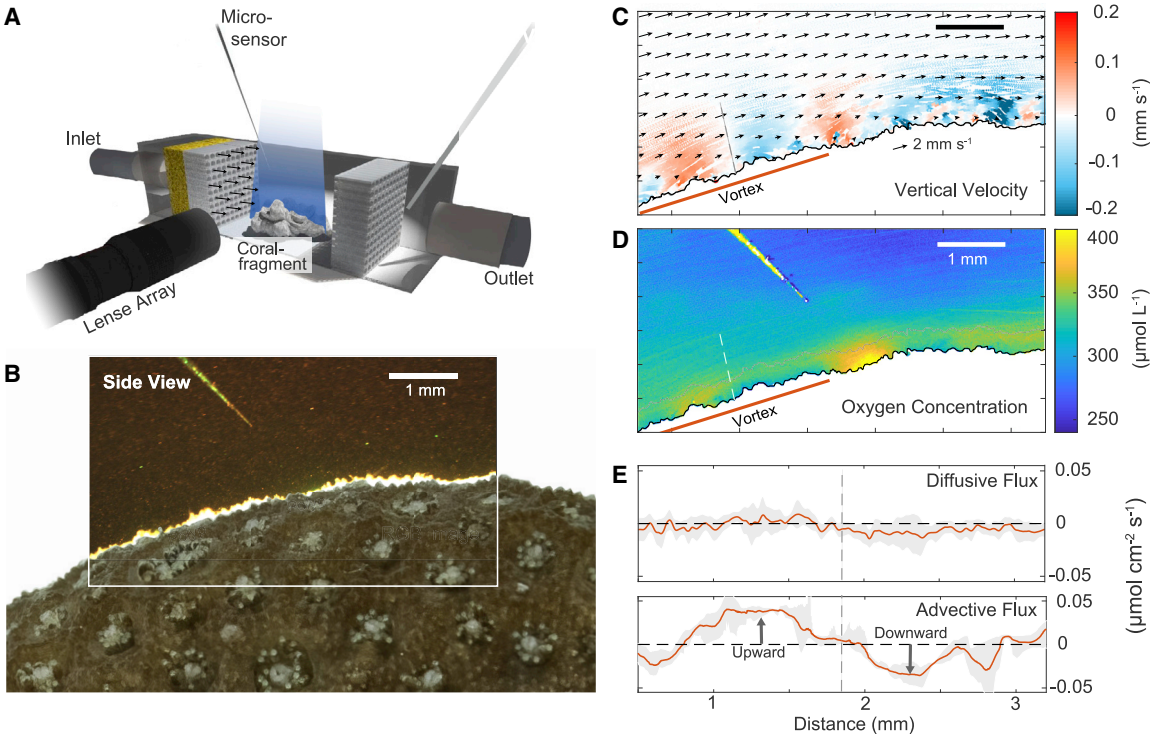

Figure 5. sensPIV can visualize flow and O_2 around corals and other complex biological structures

(A) A custom light-sheet-microscope-based flow chamber setup containing an actively stirring coral specimen (*Porites lutea*; see Video S1 for video).

(B) Color image of sensPIV particles around the coral surface. Note the O_2 microsensor in the top left corner, which is used to cross-reference measurements.

(C) Combined particle image velocimetry (PIV) and particle tracking velocimetry (PTV) graph of sensPIV particles. Arrows indicate the flow along the coral's surface, as determined by PIV using the red channel of the RGB image. Colored dots represent individual particles, and the color indicates the velocity component perpendicular to the coral surface as determined by PTV. Red and blue depict upward and downward flow of particles, respectively.

(D) sensPIV-derived O_2 concentrations inside the coral boundary layer.

(E) Diffusive and advective O_2 fluxes normal to the surface along the vortex area highlighted in (D). The advective flux perpendicular to the surface was averaged for the first 250 µm above the coral surface along the red line, and the upper limit is indicated by a gray line in (D).

approximately 10%–15% and that additional images ($n > 40$) reduced the error to below 2% (see Figure S4). To compare the accuracy of sensPIV with the accuracy of a "traditional" amperometric microsensor, individual vertical profiles were extracted from sensPIV measurements and O_2 concentrations were found to change by $\Delta C = 1.5$ µmol L^{-1} over a distance of $\sim\Delta z = 20$ µm, which is close to the resolution of commercially available O_2 microsensors (see Figure S5). However, while both methods capture similar O_2 concentrations, microsensors are able to resolve more pronounced gradients. We attribute this to the fact that the sensPIV experiments were performed at oversaturated O_2 concentrations in the range of 240–650 µmol L^{-1} (compare Nelson and Altieri, 2019). At this concentration range, the phosphorescence of O_2 sensor particles is already substantially quenched, as illustrated by the sensor calibration (Figure 1G). At an O_2 saturation of 0%, a 10% change of O_2 results in a signal change of 7%, while at 100% O_2 saturation, a 10% change of O_2 results in a signal change of 1%. PtTFPP thus appears best suited for low-O_2 conditions, and better accuracies at high O_2 concentrations could be achieved with iridium or ruthenium-based dyes (Quaranta et al., 2012).

The sensPIV analysis of O_2 concentrations revealed a boundary layer along the coral surface with a width of approximately 1,300 ± 300 µm (Figures 5D and S5C) and characterized by large heterogeneities in both horizontal and vertical directions. Two distinct semi-circular-shaped vortices indicated local increases in O_2 production at the coral surface (Figure 5D). The width of the vortices varied between 800 and 1,500 µm and extended 900 ± 300 µm into the flow field, thus traversing almost the entire boundary layer (Figure 5D). The flow field (black arrows in Figure 5C) in the vicinity of the coral exhibited complex pulsed movements that were insufficiently captured by averaged image ensembles. To improve the visualization of these vortical flows, the velocity perpendicular to the coral surface was calculated via PTV (Figure 5C). This demonstrated that vertical velocities ranged from −0.1 to 0.1 mm s^{-1} and the width of each of the vortices was 1,000–1,250 µm (compare also Figure S5D).

A comparison of O_2 concentrations and flow fields suggest that upward-directed fluid motion, induced by cilia, coincides with zones of higher O_2 concentrations while downwelling flows coincide with lower O_2 concentrations. This implies that cilia are not stirring the entire boundary layer homogeneously as assumed previously (Shapiro et al., 2014) but likely organize their beating pattern to increase the upward transport of excess O_2 from the tissue. O_2 is also transported downwards toward the mouth openings (Pacherres et al., 2022) where the coral actively

respires. SensPIV has thus helped reveal that the coral actively stirs the boundary layer in order to externally link zones of O_2 production with zones of O_2 consumption and, presumably, accelerate metabolism. To quantify this transport effect, we calculated the advective flux of O_2 as

$$J_{adv} = u_{\perp} C$$

and diffusive flux as

$$J_{diff} = -D\,\vec{n}\cdot\nabla C\,,$$

where $u_{\perp}$ is the velocity perpendicular to the surface and C is the O_2 concentration. The advective flux of O_2 was averaged for the first 250 μm above the coral surface and ranged from −36 nmol cm^{-2} s^{-1} to 38 nmol cm^{-2} s^{-1} (negative sign implies downward-pointing flux, compare Figure 5E). Averaging along the vortex, the net upward flux is 1.5 nmol cm^{-2} s^{-1}. In comparison, the net diffusive flux (averaged along the whole coral surface) is 0.4 nmol cm^{-2} s^{-1}. The dominance of advection over diffusion can be tested using the non-dimensional Peclet number $(Pe \sim u_{\perp} L/D)$, where L is the characteristic length scale of the vortices (L ≈ 1,000 μm). For the present coral, the Peclet number was calculated to be approximately 100, confirming the ratio of the measured advective to diffusive fluxes of ∼95. In conclusion, the dominance of advective fluxes implies a substantial consumption of photosynthetically produced O_2 through respiration at the mouth openings.

DISCUSSION

SensPIV links microscale measurements of flow, traditionally performed via PIV, with measurements of O_2 concentrations, typically performed with microsensors or immobilized optodes. Our three test cases demonstrate the power of sensPIV to study microscale advective and diffusive fluxes in experiments at varying complexity. These applications show the simple implementation of sensPIV for experimental research ranging from ecology to life sciences and engineering. Using sensPIV, we obtained insight into how corals optimize O_2 consumption and production by measuring their advective ciliary flow. Previously, heterogeneous nutrient and O_2 concentrations within the boundary layer of corals were attributed to changes in coral topography or flow and the resulting variations in concentration boundary layer thicknesses (de Beer et al., 2000; Shashar et al., 1993). Using sensPIV, we instead discovered that coral topography acts in tandem with local ciliary flow to enhance removal of O_2 from coral tissues and, at the same time, optimize the coral metabolism. While further research is needed to disentangle the complex interactions occurring on coral surfaces, our initial results emphasize the ability of sensPIV to provide insights into mass-flow exchange around complex biological structures. Although we only present results from the coral species *P. lutea*, we emphasize that cilia are found in many biological systems, such as in the human respiratory tract (Loiseau et al., 2020) and the oviduct of female mammals (Enuka et al., 2012; Byatt-Smith et al., 1991). In these examples, the transport of O_2 might play a key role in the clearance of particles and pathogens and for supplying O_2 to embryos, which could be studied using sensPIV.

Notably, sensPIV (in its most basic form) only requires simple setups (see key resources table), making this technology accessible to the research community at low cost. We thus anticipate the integration of sensPIV into a range of existing microscopy platforms (e.g., light-sheet microscopy; Krzic et al., 2012) or into aquatic *in situ* laser scanning instruments for measurements of O_2 and flow fields (e.g., Ahmerkamp et al., 2017; Katija et al., 2017; Liao et al., 2009; Katija and Dabiri, 2008). Moreover, engineering and medical research may also profit from sensPIV as a tool to study transport of O_2 in bioreactors (Seidel et al., 2021), for aerodynamic pressure measurements (Gregory et al., 2008), when measuring the transfer efficiency of O_2 to tissue cells (Bein et al., 2018), or even to discriminate pO_2 in cell populations via flow cytometry (e.g., Koch, 2002). To date, most studies that estimate the effect of flow on O_2 fluxes have been performed using numerical models (e.g. Moradi et al., 2018; Ahmerkamp et al., 2015; Broomé et al., 2013). However, these models are abstract versions of reality, rely on simplified system geometries and boundary conditions, usually assume immobile objects, and typically discount microscale heterogeneities in flow and O_2 concentrations. By applying sensPIV to sinking agarose aggregates, we revealed the bias resulting from model oversimplifications and highlighted the need to include the porosity of aggregates for more realistic predictions. In the future, sensPIV could probe the influence of the spatial organization of micro-organisms inside aggregates and their exchange with ambient flow and chemistry. Moreover, the combination of numerical simulations with sensPIV experiments could provide powerful insights into the complex coupling between flow, metabolic rates, and exchange fluxes. Our model aggregates (test case 2) also serve as analogs of other motile "particles," such as synthetic microswimmers or motile micro-organisms, and could facilitate measurements of O_2 "trails" around individual cells (Guasto et al., 2012; Kanso et al., 2021) and to study the collective mixing of suspensions of micro-organisms (Sommer et al., 2017). Applying sensPIV in more complex flow setups will enable the study of planktonic organisms (Krishnamurthy et al., 2020) and their single-cell heterogeneity (Behrendt et al., 2020). Understanding the dynamics underlying these processes could lead to novel insights into how organisms interact with their microscale environment.

Finally, sensPIV is not limited to measurements of O_2 but can, in principle, also measure an increasing number of other analytes including pH, CO_2, temperature, and NH_3 (Merl and Koren, 2020; Moβhammer et al., 2019). Our sensPIV data on corals emphasize the need for measuring spatially separated zones of production and consumption to understand the distribution of metabolites across complex shapes. The exchange processes between coral endosymbionts and the coral animal in the boundary layer likely apply to nutrient distributions and chemical solutes in addition to O_2. The integration of other chemical sensors into sensPIV could provide important insights into the interplay between remineralization processes and flow at the scale of individual organisms.

Limitations of the study

SensPIV has limitations that are related to current imaging technologies and synthesis of sensor particles. The spatial resolution of sensPIV is mainly limited by the size of particles and the ability of cameras to discern them as individuals. In our test cases, the

smallest visible sensor particles had a median diameter of 500 nm. Consequently, this set the resolution for resolving spatial gradients in the range of 1–10 μm. For intracellular studies, where a resolution far below 1 μm is required and diffusion timescales dominate, other methods thus far surpass the ability of sensPIV to measure O_2 concentrations (e.g., Okkelman et al., 2020; Zhdanov et al., 2015). The strength of sensPIV is its ability to image flow fields and concentrations simultaneously at a resolution that is close to microsensors. However, if the effects of flow fields are negligible and/or O_2 gradients are one-dimensional, traditional microsensors still outperform sensPIV in relation to spatial resolution and accuracy.

Further, if sensPIV is applied to autofluorescent organisms (e.g., phototrophs), their natural fluorescence can interfere with the luminescence signal emitted by sensPIV particles. This limitation can be overcome by using O_2-sensitive dyes, which are excited in the deep red or near-infrared range and thereby avoid autofluorescence spillover from photopigments (e.g., Niedermair et al., 2010). If information on O_2 concentrations within the tissue are of interest, confocal laser scanning microscopy or two-photon phosphorescence lifetime microscopy may be a powerful alternative to sensPIV (see, e.g., Shen et al., 2018 and Moritomo et al., 2016). Finally, during the synthesis of sensor particles, the amount of dye embedded within individual sensor particles can vary. This can affect luminescence intensities and the ratiometric signal at constant O_2 concentrations (visible in Figure S3B) and requires compensation by averaging spatially or across image ensembles. Particle synthesis can also be improved through the covalent coupling of PtTFPP and the reference dye (e.g., Koren et al., 2012), resulting in improved resonance energy transfer and an improved referencing in ratiometric imaging approaches.

STAR★METHODS

Detailed methods are provided in the online version of this paper and include the following:

- KEY RESOURCES TABLE
- RESOURCE AVAILABILITY
  - Lead contact
  - Materials availability
  - Data and code availability
- EXPERIMENTAL MODEL AND SUBJECT DETAILS
- METHOD DETAILS
  - Sensor particle production
  - Exciting and measuring sensPIV particles
  - SensPIV under well-defined O_2 gradients within microfluidic devices
  - Measuring the dynamic O_2 exchange around a model laboratory aggregate
  - SensPIV for the visualization of O_2 dynamics and vortical flows around the coral *P. lutea*
- QUANTIFICATION AND STATISTICAL ANALYSIS

SUPPLEMENTAL INFORMATION

Supplemental information can be found online at https://doi.org/10.1016/j.crmeth.2022.100216.

ACKNOWLEDGMENTS

We thank Volker Meyer, Paul Faerber, and Gerhard Holst for technical support. We thank Claudio Richter for providing the coral *Porites lutea*. We thank Sina Schorn, Bram Vekeman, and Juliane Schoetz for support in the laboratory. We thank Dirk de Beer for valuable discussions and comments. D.R.B. was supported by an Australian Research Council (ARC) Discovery Early Career Researcher Award DE180100911 and a Gordon & Betty Moore Foundation Symbiosis in Aquatic Systems grant. C.O.P. acknowledges funding from the Helmholtz Association (Alfred Wegener Institute, Helmholtz Center for Polar and Marine Research). F.M.J. received funding from the Cluster of Excellence "The Ocean Floor—Earth's Uncharted Interface" (Germany's Excellence Strategy-EXC-2077-390741603 of the DFG). L.B. and Y.C. were supported by grants from the Swedish Research Council (2019-04401) and the Science for Life Laboratory. R.S. acknowledges funding from the Simons Foundation through the Principles of Microbial Ecosystems (PriME) Collaborative (grant 542395). RS acknowledges support from a Symbiosis in Aquatic Systems Investigator Award from the Gordon and Betty Moore Foundation (GBMF9197; https://doi.org/10.37807/GBMF9197). K.K. acknowledges financial support by research grants from the Grundfos Foundation and a Sapere Aude grant from the Independent Research Fund Denmark (IRFD): DFF-8048-00057B. The study was funded by the Max Planck Society (MPG) through the "Multiscale Approach on the Role of Marine Aggregates" (MARMA) project.

AUTHOR CONTRIBUTIONS

S.A., L.B., K.K., M.M.M.K., J.B., D.R.B., and R.S. conceived the study and interpreted data. K.K. synthesized sensor particles. Y.C. and L.B. performed experiments with microfluidic chips and processed data. F.M.J. and S.A. performed experiments with laboratory particles and processed data. S.A. developed and built optical setups. C.O.P. and S.A. developed flow-chamber setup, performed experiments with coral fragments, and processed data. C.O.P. performed microsensor measurement. All authors edited and approved the paper.

DECLARATION OF INTERESTS

The authors declare no competing interests.

Received: January 5, 2022
Revised: March 5, 2022
Accepted: April 20, 2022
Published: May 23, 2022

REFERENCES

Abe, S., Okamoto, K., and Madarame, H. (2004). The development of PIV–PSP hybrid system using pressure sensitive particles. Meas. Sci. Technol. *15*, 1153–1157. https://doi.org/10.1088/0957-0233/15/6/016.

Ahmerkamp, S., Winter, C., Janssen, F., Kuypers, M.M.M., and Holtappels, M. (2015). The impact of bedform migration on benthic oxygen fluxes. J. Geophys. Res. Biogeosci. *120*, 2229–2242. https://doi.org/10.1002/2015jg003106.

Ahmerkamp, S., Winter, C., Krämer, K., Beer, D.D., Janssen, F., Friedrich, J., Kuypers, M.M.M., and Holtappels, M. (2017). Regulation of benthic oxygen fluxes in permeable sediments of the coastal ocean. Limnol. Oceanogr. *62*, 1935–1954. https://doi.org/10.1002/lno.10544.

Batchelor, G.K. (2000). An Introduction to Fluid Dynamics (Cambridge University Press).

Behrendt, L., Salek, M.M., Trampe, E.L., Fernandez, V.I., Lee, K.S., Kühl, M., and Stocker, R. (2020). PhenoChip: a single-cell phenomic platform for high-throughput photophysiological analyses of microalgae. Sci. Adv. *6*, eabb2754. https://doi.org/10.1126/sciadv.abb2754.

Bein, A., Shin, W., Jalili-Firoozinezhad, S., Park, M.H., Sontheimer-Phelps, A., Tovaglieri, A., Chalkiadaki, A., Kim, H.J., and Ingber, D.E. (2018). Microfluidic

organ-on-a-chip models of human intestine. Cell Mol. Gastroenterol. Hepatol. *5*, 659–668. https://doi.org/10.1016/j.jcmgh.2017.12.010.

Bekker, A., Holland, H.D., Wang, P.L., Rumble, D.I.I.I., Stein, H.J., Hannah, J.L., Coetzee, L.L., and Beukes, N.J. (2004). Dating the rise of atmospheric oxygen. Nature *427*, 117–120. https://doi.org/10.1038/nature02260.

Bianchi, D., Weber, T.S., Kiko, R., and Deutsch, C. (2018). Global niche of marine anaerobic metabolisms expanded by particle microenvironments. Nat. Geosci. *11*, 263–268. https://doi.org/10.1038/s41561-018-0081-0.

Borisov, S.M., Mayr, T., and Klimant, I. (2008). Poly (styrene-block-vinylpyrrolidone) beads as a versatile material for simple fabrication of optical nanosensors. Anal. Chem. *80*, 573–582. https://doi.org/10.1021/ac071374e.

Broomé, M., Maksuti, E., Bjällmark, A., Frenckner, B., and Janerot-Sjöberg, B. (2013). Closed-loop real-time simulation model of hemodynamics and oxygen transport in the cardiovascular system. Biomed. Eng. Online *12*, 69. https://doi.org/10.1186/1475-925x-12-69.

Byatt-Smith, J.G., Leese, H.J., and Gosden, R.G. (1991). An investigation by mathematical modelling of whether mouse and human preimplantation embryos in static culture can satisfy their demands for oxygen by diffusion. Hum. Reprod. *6*, 52–57. https://doi.org/10.1093/oxfordjournals.humrep.a137258.

Chen, H., Holst, G., and Gratton, E. (2015). Modulated CMOS camera for fluorescence lifetime microscopy. Microsc. Res. Tech. *78*, 1075–1081. https://doi.org/10.1002/jemt.22587.

Clark, L.C., JR., Wolf, R., Granger, D., and Taylor, Z. (1953). Continuous recording of blood oxygen tensions by polarography. J. Appl. Physiol. *6*, 189–193. https://doi.org/10.1152/jappl.1953.6.3.189.

Costello, J.H., Colin, S.P., Dabiri, J.O., Gemmell, B.J., Lucas, K.N., and Sutherland, K.R. (2021). The hydrodynamics of jellyfish swimming. Annu. Rev. Mar. Sci. *13*, 375–396. https://doi.org/10.1146/annurev-marine-031120-091442.

de Beer, D., Kühl, M., Stambler, N., and Vaki, L. (2000). A microsensor study of light enhanced Ca2+ uptake and photosynthesis in the reef-building hermatypic coral Favia sp. Mar. Ecol. Prog. Ser. *194*, 75–85. https://doi.org/10.3354/meps194075.

Drescher, K., Goldstein, R.E., Michel, N., Polin, M., and Tuval, I. (2010). Direct measurement of the flow field around swimming microorganisms. Phys. Rev. Lett. *105*, 168101. https://doi.org/10.1103/physrevlett.105.168101.

Enuka, Y., Hanukoglu, I., Edelheit, O., Vaknine, H., and Hanukoglu, A. (2012). Epithelial sodium channels (ENaC) are uniformly distributed on motile cilia in the oviduct and the respiratory airways. Histochem. Cell Biol. *137*, 339–353. https://doi.org/10.1007/s00418-011-0904-1.

Fabricius-Dyg, J., Mistlberger, G., Staal, M., Borisov, S.M., Klimant, I., and Kühl, M. (2012). Imaging of surface O2 dynamics in corals with magnetic micro optode particles. Mar. Biol. *159*, 1621–1631. https://doi.org/10.1007/s00227-012-1920-y.

Falkowski, P.G. (2006). Tracing oxygen's imprint on earth's metabolic evolution. Science *311*, 1724–1725. https://doi.org/10.1126/science.1125937.

Frederiksen, M.S., and Glud, R.N. (2006). Oxygen dynamics in the rhizosphere of Zostera marina: a two dimensional planar optode study. Limnol. Oceanogr. *51*, 1072–1083. https://doi.org/10.4319/lo.2006.51.2.1072.

Garren, M., Son, K., Raina, J.B., Rusconi, R., Menolascina, F., Shapiro, O.H., Tout, J., Bourne, D.G., Seymour, J.R., and Stocker, R. (2014). A bacterial pathogen uses dimethylsulfoniopropionate as a cue to target heat-stressed corals. ISME J. *8*, 999–1007. https://doi.org/10.1038/ismej.2013.210.

Gemmell, B.J., Jiang, H., and Buskey, E.J. (2014). A new approach to microscale particle image velocimetry (μPIV) for quantifying flows around free-swimming zooplankton. J. Plankton Res. *36*, 1396–1401. https://doi.org/10.1093/plankt/fbu067.

Gemmell, B.J., Colin, S.P., Costello, J.H., and Dabiri, J.O. (2015). Suction-based propulsion as a basis for efficient animal swimming. Nat. Commun. *6*, 8790. https://doi.org/10.1038/ncomms9790.

Gilpin, W., Prakash, V.N., and Prakash, M. (2017). Vortex arrays and ciliary tangles underlie the feeding–swimming trade-off in starfish larvae. Nat. Phys. *13*, 380–386. https://doi.org/10.1038/nphys3981.

Gilpin, W., Bull, M.S., and Prakash, M. (2020). The multiscale physics of cilia and flagella. Nat. Rev. Phys. *2*, 74–88. https://doi.org/10.1038/s42254-019-0129-0.

Gregory, J.W., Asai, K., Kameda, M., Liu, T., and Sullivan, J.P. (2008). A review of pressure-sensitive paint for high-speed and unsteady aerodynamics. Proc. Inst. Mech. Eng. G: J. Aerospace Eng. *222*, 249–290. https://doi.org/10.1243/09544100jaero243.

Guasto, J.S., Rusconi, R., and Stocker, R. (2012). Fluid mechanics of planktonic microorganisms. Annu. Rev. Fluid Mech. *44*, 373–400. https://doi.org/10.1146/annurev-fluid-120710-101156.

Holst, G.A., Franke, U., and Grunwald, B.. Transparent oxygen optodes in environmental applications at fine scale as measured by luminescence lifetime imaging. https://www.spiedigitallibrary.org/conference-proceedings-of-spie/4576/1/Transparent-oxygen-optodes-in-environmental-applications-at-fine-scale-as/10.1117/12.456961.full.

Kanso, E.A., Lopes, R.M., Strickler, J.R., Dabiri, J.O., and Costello, J.H. (2021). Teamwork in the viscous oceanic microscale. Proc. Natl. Acad. Sci. U S A *118*. https://doi.org/10.1073/pnas.2018193118.

Karthäuser, C., Ahmerkamp, S., Marchant, H.K., Bristow, L.A., Hauss, H., Iversen, M.H., Kiko, R., Maerz, J., Lavik, G., and Kuypers, M.M.M. (2021). Small sinking particles control anammox rates in the Peruvian oxygen minimum zone. Nat. Commun. *12*, 3235. https://doi.org/10.1038/s41467-021-23340-4.

Katija, K., and Dabiri, J.O. (2008). In situ field measurements of aquatic animal fluid interactions using a Self Contained Underwater Velocimetry Apparatus (SCUVA). Limnol. Oceanogra.: Methods *6*, 162–171. https://doi.org/10.4319/lom.2008.6.162.

Katija, K., Sherlock, R.E., Sherman, A.D., and Robison, B.H. (2017). New technology reveals the role of giant larvaceans in oceanic carbon cycling. Sci. Adv. *3*, e1602374. https://doi.org/10.1126/sciadv.1602374.

Kheradvar, A., Houle, H., Pedrizzetti, G., Tonti, G., Belcik, T., Ashraf, M., Lindner, J.R., Gharib, M., and Sahn, D. (2010). Echocardiographic particle image velocimetry: a novel technique for quantification of left ventricular blood vorticity pattern. J. Am. Soc. Echocardiogr. *23*, 86–94. https://doi.org/10.1016/j.echo.2009.09.007.

Khosravi, Y., Kandukuri, R.D., Palmer, S.R., Gloag, E.S., Borisov, S.M., Starke, E.M., Ward, M.T., Kumar, P., De Beer, D., Chennu, A., and Stoodley, P. (2020). Use of an oxygen planar optode to assess the effect of high velocity microsprays on oxygen penetration in a human dental biofilms in-vitro. BMC Oral Health *20*, 230. https://doi.org/10.1186/s12903-020-01217-0.

Kim, H.D., Yi, S.J., and Kim, K.C. (2013). Simultaneous measurement of dissolved oxygen concentration and velocity field in microfluidics using oxygen-sensitive particles. Microfluidics and Nanofluidics *15*, 139–149. https://doi.org/10.1007/s10404-012-1130-4.

Kiørboe, T., and Thygesen, U.H. (2001). Fluid motion and solute distribution around sinking aggregates. II. Implications for remote detection by colonizing zooplankters. Mar. Ecol. Prog. Ser. *211*, 15–25. https://doi.org/10.3354/meps211015.

Klimant, I., Meyer, V., and Kühl, M. (1995). Fiber-optic oxygen microsensors, a new tool in aquatic biology. Limnol. Oceanogr. *40*, 1159–1165. https://doi.org/10.4319/lo.1995.40.6.1159.

Koch, C.J. (2002). Measurement of absolute oxygen levels in cells and tissues using oxygen sensors and 2-nitroimidazole EF5. Methods Enzymol. *352*, 3–31. SSN 0076-6879.

Koren, K., Borisov, S.M., and Klimant, I. (2012). Stable optical oxygen sensing materials based on click-coupling of fluorinated platinum (II) and palladium (II) porphyrins—a convenient way to eliminate dye migration and leaching. Sensors Actuators B: Chem. *169*, 173–181. https://doi.org/10.1016/j.snb.2012.04.062.

Koren, K., Brodersen, K.E., Jakobsen, S.L., and Kühl, M. (2015). Optical sensor nanoparticles in artificial sediments–a new tool to visualize O2 dynamics around the rhizome and roots of seagrasses. Environ. Sci. Technol. *49*, 2286–2292. https://doi.org/10.1021/es505734b.

Koren, K., Jakobsen, S.L., and Kühl, M. (2016). In-vivo imaging of O2 dynamics on coral surfaces spray-painted with sensor nanoparticles. Sensors Actuators B: Chem. *237*, 1095–1101. https://doi.org/10.1016/j.snb.2016.05.147.

Koren, K., Moßhammer, M., Scholz, V.V., Borisov, S.M., Holst, G., and Kühl, M. (2019). Luminescence lifetime imaging of chemical sensors - a comparison between time-domain and frequency-domain based camera systems. Anal. Chem. *91*, 3233–3238. https://doi.org/10.1021/acs.analchem.8b05869.

Krishnamurthy, D., Li, H., Benoit du Rey, F., Cambournac, P., Larson, A.G., Li, E., and Prakash, M. (2020). Scale-free vertical tracking microscopy. Nat. Methods *17*, 1040–1051. https://doi.org/10.1038/s41592-020-0924-7.

Krzic, U., Gunther, S., Saunders, T.E., Streichan, S.J., and Hufnagel, L. (2012). Multiview light-sheet microscope for rapid in toto imaging. Nat. Methods *9*, 730–733. https://doi.org/10.1038/nmeth.2064.

Kühl, M., Trampe, E., Mosshammer, M., Johnson, M., Larkum, A.W., Frigaard, N.U., and Koren, K. (2020). Substantial near-infrared radiation-driven photosynthesis of chlorophyll f-containing cyanobacteria in a natural habitat. Elife *9*, e50871. https://doi.org/10.7554/elife.50871.

Liao, Q., Bootsma, H.A., Xiao, J., Klump, J.V., Hume, A., Long, M.H., and Berg, P. (2009). Development of an in situ underwater particle image velocimetry (UWPIV) system. Limnol. Oceanogr.: Methods *7*, 169–184. https://doi.org/10.4319/lom.2009.7.169.

Loiseau, E., Gsell, S., Nommick, A., Jomard, C., Gras, D., Chanez, P., D'ortona, U., Kodjabachian, L., Favier, J., and Viallat, A. (2020). Active mucus–cilia hydrodynamic coupling drives self-organization of human bronchial epithelium. Nat. Phys. *16*, 1158–1164. https://doi.org/10.1038/s41567-020-0980-z.

Markov, D.A., Lillie, E.M., Garbett, S.P., and McCawley, L.J. (2014). Variation in diffusion of gases through PDMS due to plasma surface treatment and storage conditions. Biomed. Microdevices *16*, 91–96. https://doi.org/10.1007/s10544-013-9808-2.

Mayr, T., Borisov, S.M., Abel, T., Enko, B., Waich, K., Mistlberger, G., and Klimant, I. (2009). Light harvesting as a simple and versatile way to enhance brightness of luminescent sensors. Anal. Chem. *81*, 6541–6545. https://doi.org/10.1021/ac900662x.

Menolascina, F., Rusconi, R., Fernandez, V.I., Smriga, S., Aminzare, Z., Sontag, E.D., and Stocker, R. (2017). Logarithmic sensing in Bacillus subtilis aerotaxis. NPJ Syst. Biol. Appl. *3*, 16036. https://doi.org/10.1038/npjsba.2016.36.

Merl, T., and Koren, K. (2020). Visualizing NH3 emission and the local O2 and pH microenvironment of soil upon manure application using optical sensors. Environ. Int. *144*, 106080. https://doi.org/10.1016/j.envint.2020.106080.

Meysman, F.J.R., Galaktionov, O.S., Glud, R.N., and Middelburg, J.J. (2010). Oxygen penetration around burrows and roots in aquatic sediments. J. Mar. Res. *68*, 309–336. https://doi.org/10.1357/002224010793721406.

Mistlberger, G., Koren, K., Scheucher, E., Aigner, D., Borisov, S.M., Zankel, A., Pölt, P., and Klimant, I. (2010). Multifunctional magnetic optical sensor particles with tunable sizes for monitoring metabolic parameters and as a basis for nanotherapeutics. Adv. Funct. Mater. *20*, 1842–1851. https://doi.org/10.1002/adfm.201000321.

Moradi, N., Liu, B., Iversen, M., Kuypers, M.M., Ploug, H., and Khalili, A. (2018). A new mathematical model to explore microbial processes and their constraints in phytoplankton colonies and sinking marine aggregates. Sci. Adv. *4*, eaat1991. https://doi.org/10.1126/sciadv.aat1991.

Moritomo, H., Fujii, A., Suzuki, Y., Yoshihara, T., Tobita, S., and Kawamata, J. (2016). Biological oxygen sensing via two-photon absorption by an Ir (III) complex using a femtosecond fiber laser. Jpn. J. Appl. Phys. *55*, 092401. https://doi.org/10.7567/jjap.55.092401.

Morris, M.J., Donovan, J.F., Kegelman, J.T., Schwab, S.D., Levy, R.L., and Crites, R.C. (1993). Aerodynamic applications of pressure sensitive paint. AIAA J. *31*, 419–425. https://doi.org/10.2514/3.11346.

Moßhammer, M., Brodersen, K.E., Kühl, M., and Koren, K. (2019). Nanoparticle-and microparticle-based luminescence imaging of chemical species and temperature in aquatic systems: a review. Microchim. Acta *186*, 126. https://doi.org/10.1007/s00604-018-3202-y.

Murniati, E., Gross, D., Herlina, H., Hancke, K., Glud, R.N., and Lorke, A. (2016). Oxygen imaging at the sediment water interface using lifetime based laser induced fluorescence (τLIF) of nano-sized particles. Limnol. Oceanogr.: Methods *14*, 506–517. https://doi.org/10.1002/lom3.10108.

Nelson, H.R., and Altieri, A.H. (2019). Oxygen: the universal currency on coral reefs. Coral Reefs *38*, 177–198. https://doi.org/10.1007/s00338-019-01765-0.

Niedermair, F., Borisov, S.M., Zenkl, G., Hofmann, O.T., Weber, H., Saf, R., and Klimant, I. (2010). Tunable phosphorescent NIR oxygen indicators based on mixed benzo-and naphthoporphyrin complexes. Inorg. Chem. *49*, 9333–9342. https://doi.org/10.1021/ic100955z.

Nielsen, L.T., and Kiørboe, T. (2021). Foraging trade-offs, flagellar arrangements, and flow architecture of planktonic protists. Proc. Natl. Acad. Sci. U S A. *118*. https://doi.org/10.1073/pnas.2009930118.

Okkelman, I.A., Neto, N., Papkovsky, D.B., Monaghan, M.G., and Dmitriev, R.I. (2020). A deeper understanding of intestinal organoid metabolism revealed by combining fluorescence lifetime imaging microscopy (FLIM) and extracellular flux analyses. Redox Biol. *30*, 101420. https://doi.org/10.1016/j.redox.2019.101420.

Ouellette, N.T., Xu, H., and Bodenschatz, E. (2006). A quantitative study of three-dimensional Lagrangian particle tracking algorithms. Exp. Fluids *40*, 301–313. https://doi.org/10.1007/s00348-005-0068-7.

Pacherres, C.O., Schmidt, G.M., and Richter, C. (2013). Autotrophic and heterotrophic responses of the coral Porites lutea to large amplitude internal waves. J. Exp. Biol. *216*, 4365–4374. https://doi.org/10.1242/jeb.085548.

Pacherres, C.O., Ahmerkamp, S., Schmidt-Grieb, G.M., Holtappels, M., and Richter, C. (2020). Ciliary vortex flows and oxygen dynamics in the coral boundary layer. Scientific Rep. *10*, 7541. https://doi.org/10.1038/s41598-020-64420-7.

Pacherres, C.O., Ahmerkamp, S., Koren, K., Richter, C., and Holtappels, M. (2022). Ciliary flows in corals ventilate target areas of high photosynthetic oxygen production. Sci Rep. *10*, 7541. https://doi.org/10.2139/ssrn.4058690.

Pedersen, O., Borum, J., Duarte, C.M., and Fortes, M.D. (1998). Oxygen dynamics in the rhizosphere of Cymodocea rotundata. Mar. Ecol. Prog. Ser. *169*, 283–288. https://doi.org/10.3354/meps169283.

Ploug, H. (2001). Small scale oxygen fluxes and remineralization in sinking aggregates. Limnol. Oceanogr. *46*, 1624–1631. https://doi.org/10.4319/lo.2001.46.7.1624.

Quaranta, M., Borisov, S.M., and Klimant, I. (2012). Indicators for optical oxygen sensors. Bioanal. Rev. *4*, 115–157. https://doi.org/10.1007/s12566-012-0032-y.

Raffel, M., Willert, C.E., and Kompenhans, J. (1998). Particle Image Velocimetry: A Practical Guide, *2* (Springer).

Revsbech, N.P., and Jørgensen, B.B. (1986). Microelectrodes: their use in microbial ecology. In Advances in Microbial Ecology (Springer), pp. 293–352.

Rusconi, R., Garren, M., and Stocker, R. (2014a). Microfluidics expanding the frontiers of microbial ecology. Annu. Rev. Biophys. *43*, 65–91. https://doi.org/10.1146/annurev-biophys-051013-022916.

Rusconi, R., Guasto, J.S., and Stocker, R. (2014b). Bacterial transport suppressed by fluid shear. Nat. Phys. *10*, 212–217. https://doi.org/10.1038/nphys2883.

Schindelin, J., Arganda-Carreras, I., Frise, E., Kaynig, V., Longair, M., Tobias, P., Preibisch, S., Rueden, C., Saalfeld, S., Schmid, B., et al. (2012). Fiji: an open-source platform for biological-image analysis. Nat. Methods *9*, 676–682. https://doi.org/10.1038/nmeth.2019.

Seidel, S., Maschke, R.W., Werner, S., Jossen, V., and Eibl, D. (2021). Oxygen mass transfer in biopharmaceutical processes: numerical and experimental approaches. Chem. Ingenieur Technik *93*, 42–61. https://doi.org/10.1002/cite.202000179.

Shapiro, O.H., Fernandez, V.I., Garren, M., Guasto, J.S., Debaillon-Vesque, F.P., Kramarsky-Winter, E., Vardi, A., and Stocker, R. (2014). Vortical ciliary flows actively enhance mass transport in reef corals. Proc. Natl. Acad. Sci.U S A *111*, 13391–13396. https://doi.org/10.1073/pnas.1323094111.

Shashar, N., Cohen, Y., and Loya, Y. (1993). Extreme diel fluctuations of oxygen in diffusive boundary layers surrounding stony corals. Biol Bull *185*, 455–461.

Sheffield, P.J. (1998). Measuring tissue oxygen tension: a review. Undersea Hyperb. Med. *25*, 179–188.

Shen, N., Riedl, J.A., Carvajal Berrio, D.A., Davis, Z., Monaghan, M.G., Layland, S.L., Hinderer, S., and Schenke-Layland, K. (2018). A flow bioreactor system compatible with real-time two-photon fluorescence lifetime imaging microscopy. Biomed. Mater. *13*, 024101. https://doi.org/10.1088/1748-605x/aa9b3c.

Sleigh, M.A. (1962). The Biology of Cilia and Flagella: International Series of Monographs on Pure and Applied Biology: Zoology, *12* (Elsevier).

Sommer, T., Danza, F., Berg, J., Sengupta, A., Constantinescu, G., Tokyay, T., Bürgmann, H., Dressler, Y., Sepúlveda Steiner, O., Schubert, C.J., et al. (2017). Bacteria-induced mixing in natural waters. Geophys. Res. Lett. *44*, 9424–9432. https://doi.org/10.1002/2017gl074868.

Son, K., Brumley, D.R., and Stocker, R. (2015). Live from under the lens: exploring microbial motility with dynamic imaging and microfluidics. Nat. Rev. Microbiol. *13*, 761–775. https://doi.org/10.1038/nrmicro3567.

Spencer, J.A., Ferraro, F., Roussakis, E., Klein, A., Wu, J., Runnels, J.M., Zaher, W., Mortensen, L.J., Alt, C., Turcotte, R., et al. (2014). Direct measurement of local oxygen concentration in the bone marrow of live animals. Nature *508*, 269–273. https://doi.org/10.1038/nature13034.

Speth, D.R., In 't Zandt, M.H., Guerrero-Cruz, S., Dutilh, B.E., Jetten, M.S.M., and Jetten, M.S. (2016). Genome-based microbial ecology of anammox granules in a full-scale wastewater treatment system. Nat. Commun. *7*, 11172. https://doi.org/10.1038/ncomms11172.

Stockdale, A., Davison, W., and Zhang, H. (2009). Micro-scale biogeochemical heterogeneity in sediments: a review of available technology and observed evidence. Earth-Science Rev. *92*, 81–97. https://doi.org/10.1016/j.earscirev.2008.11.003.

Stocker, R. (2012). Marine microbes see a sea of gradients. science *338*, 628–633. https://doi.org/10.1126/science.1208929.

Tobita, S., and Yoshihara, T. (2016). Intracellular and in vivo oxygen sensing using phosphorescent iridium (III) complexes. Curr. Opin. Chem. Biol. *33*, 39–45. https://doi.org/10.1016/j.cbpa.2016.05.017.

Trampe, E., Koren, K., Akkineni, A.R., Senwitz, C., Krujatz, F., Lode, A., Gelinsky, M., and Kühl, M. (2018). Functionalized bioink with optical sensor nanoparticles for O2 imaging in 3Dbioprinted constructs. Adv. Funct. Mater. *28*, 1804411. https://doi.org/10.1002/adfm.201804411.

Wan, K.Y. (2018). Coordination of eukaryotic cilia and flagella. Essays Biochem. *62*, 829–838. https://doi.org/10.1042/ebc20180029.

Wang, X.D., and Wolfbeis, O.S. (2014). Optical methods for sensing and imaging oxygen: materials, spectroscopies and applications. Chem. Soc. Rev. *43*, 3666–3761. https://doi.org/10.1039/c4cs00039k.

Westerweel, J., Elsinga, G.E., and Adrian, R.J. (2013). Particle image velocimetry for complex and turbulent flows. Annu. Rev. Fluid Mech. *45*, 409–436. https://doi.org/10.1146/annurev-fluid-120710-101204.

Willert, C., Stasicki, B., Klinner, J., and Moessner, S. (2010). Pulsed operation of high-power light emitting diodes for imaging flow velocimetry. Meas. Sci. Technol. *21*, 075402. https://doi.org/10.1088/0957-0233/21/7/075402.

Yawata, Y., Cordero, O.X., Menolascina, F., Hehemann, J.H., Polz, M.F., and Stocker, R. (2014). Competition–dispersal tradeoff ecologically differentiates recently speciated marine bacterioplankton populations. Proc. Natl. Acad. Sci.U S A. *111*, 5622–5627. https://doi.org/10.1073/pnas.1318943111.

Yousif, M.Y., Holdsworth, D.W., and Poepping, T.L. (2011). A blood-mimicking fluid for particle image velocimetry with silicone vascular models. Experiments in fluids *50*, 769–774. https://doi.org/10.1007/s00348-010-0958-1.

Zetsche, E.M., Larsson, A.I., Iversen, M.H., and Ploug, H. (2020). Flow and diffusion around and within diatom aggregates: effects of aggregate composition and shape. Limnol. Oceanogr. *65*, 1818–1833. https://doi.org/10.1002/lno.11420.

Zhdanov, A.V., Golubeva, A.V., Okkelman, I.A., Cryan, J.F., and Papkovsky, D.B. (2015). Imaging of oxygen gradients in giant umbrella cells: an ex vivo PLIM study. Am. J. Physiology-Cell Physiol. *309*, C501–C509. https://doi.org/10.1152/ajpcell.00121.2015.

STAR★METHODS

KEY RESOURCES TABLE

REAGENT or RESOURCE	SOURCE	IDENTIFIER
Chemicals, peptides, and recombinant proteins		
Acetone	Sigma-Aldrich	Cat# 179124
Tetrahydrofuran	Sigma-Aldrich	Cat# 360589
Agarose	Biozym	Cat# 840004
Platinum(II) meso- (2,3,4,5,6-pentafluoro)phenyl porphyrin	Frontier Scientific	Cat# PtT975
Macrolex fluorescence yellow 10GN	Lanxess	Cat# 05-2114486485-35–0000
Polymer Styrene Maleic Anhydride copolymer	Polyscope, XIRAN®	N/A
Microspheres	FluoSpheres	Cat# F13080
Experimental models: Organisms/strains		
Porites lutea	Alfred Wegener Institute, Claudio Richter, (Pacherres et al., 2013)	N/A
Software and algorithms		
Lagrangian particle tracking	Ouellette et al. (2006)	https://web.stanford.edu/~nto/LPT.shtml
sensPIV processing	This paper	https://doi.org/10.6084/m9.figshare.19614273.v1
Matlab 2020b	Mathworks	https://de.mathworks.com
Adobe Creative Cloud	Adobe	https://www.adobe.com
Comsol Multiphysics v5.1	Comsol	http://www.comsol.com
PivTec v3.9	PivTec	https://www.pivtec.com
Fiji image processing v2.0	Schindelin et al. (2012)	https://imagej.net/software/fiji/
Other		
Monochromatic sCmos camera	Zyla	N/A
RGB cmos camera	Flir	GS3-U3-51S5C-C
Multi-tap camera	PCO AG	PCO.Flim
Telecentric lens	Computar	TEC – v7x
Lens array	Optem-Fusion	N/A
Microscope LED light source	Lumencor	spectraX
LED pulsing system	ILA	LPS3
Led HUB	Omicron	LedHUB
Optode Microsensor	Pyroscience	OCR430-HS
Electrochemical Microsensor	Unisense	OX-50
Linear Drive	Faulhaber	T- LSR75A
Gear Pump	Ismatec	ISM901B
100 μm Plankton Mesh	Hydro-Bios	N/A
Polyester Optical Filters	Lee Filters	010 Medium Yellow

RESOURCE AVAILABILITY

Lead contact

Further information and requests for resources and reagents should be directed to and will be fulfilled by the lead contact, Soeren Ahmerkamp (sahmerka@mpi-bremen.de).

Materials availability

This study did not generate new unique reagents.

Data and code availability

- All data reported in this paper will be shared by the lead contact upon request. Raw data are available in the supplemental information and as supplementary videos.
- Links to programs and codes are provided in the key resources table (DOI: https://doi.org/10.6084/m9.figshare.19614273.v1).
- Any additional information required to reanalyze the data reported in this paper is available from the lead contact upon request.

EXPERIMENTAL MODEL AND SUBJECT DETAILS

P. lutea colonies reared at the aquaria facilities of the Alfred Wegener Institute were used as fragment source. The colonies were kept in artificial seawater (salinity 32.6 ± 0.26) (Dupla Marine Premium Reef Salt Natural Balance), under 25.2 ± 0.07°C temperature, a 12-h light-dark cycle, light intensity of 75 and 80 μmol quanta m^{-2} s^{-1} (LI-COR LI-192, USA) and pH of 7.9 ± 0.09 (YSI, USA). Food was provided in the form of freshly hatched *Artemia nauplii* every second day. Before the start of the experiments, small fragments (1.5 cm long, 1 cm wide) were cut out from the source colonies and allowed to heal for at least two weeks in the culturing tank.

METHOD DETAILS

Sensor particle production

For ratiometric and lifetime imaging, sensor particles were prepared as described earlier via precipitation (Mistlberger et al., 2010; Koren et al., 2015, 2016) with minor specific modifications as described in the following. Briefly, 100 mg of the polymer PSMA (styrene maleic anhydride copolymer with 8% MA, Mw: 250000 g mol^{-1}; generously provided by Polyscope), 1.5 mg of the reference dye Macrolex fluorescence yellow 10GN (MY) obtained from Lanxess (Köln, Germany) and 1.5 mg of the O_2 indicator Platinum(II) meso- (2,3,4,5,6-pentafluoro)phenyl porphyrin (PtTFPP, Frontier Scientific) were dissolved in 10 g of tetrahydrofuran (THF). This solution was then rapidly poured into 200 mL of vigorously stirred MQ water. After evaporating the THF under an airstream, the particle suspension was further concentrated at elevated temperature (around 60°C) until a concentration of 5 mg mL^{-1} was reached. The final concentration was measured by drying and subsequent weighing of 1 mL of the particle suspension. A small sample was dried on an indium tin oxide coated glass slide for further inspection using a scanning electron microscope (FEI, Quanta 250 FEG scanning electron microscope) combined with a fluorescence microscope (Seacom, Delmic, Netherlands). It was ensured, that fluorescent signals based on a 392 nm excitation strongly correlated with the particles' positions on the glass side (Figure 1A).

Alternatively, particles were prepared by staining FluoSpheres™ Polystyrene Microspheres (Thermo Scientific; catalogue number F13080). One milliliter of the bead suspension was mixed with 1 mL of acetone (Sigma Aldrich) for a duration of 2 min. Afterwards, 1 mg mL^{-1} PtTFPP dissolved in acetone was added and mixed for another 2 min. Subsequently, the acetone was slowly removed from the solution by gently blowing nitrogen over the stirred solution. While the acetone evaporated, the dye became entrapped within the particles.

In all test cases, particles were centrifuged before each use. For this purpose, sensor particles at the target concentration were placed in centrifugation vessels containing the medium of the experiments. Sensor particles were then centrifuged at 3000 rpm for 5 min. For coral experiments, the sensor particles were repeatedly centrifuged in the seawater medium at a salinity of 33 PSU. Prior to experiments, the vessels were sonicated for 2 min to avoid larger aggregates. For microfluidic experiments, the supernatant was replaced with MQ water with 0.05% surfactant (Tween 20, Sigma-Aldrich Co., Germany). Before sensor particles were injected into the system, they were sonicated for 15 min to decrease aggregate formation. Producing particles with the precipitation and staining method results in a large variety of particle sizes. To optimize the size distribution, the sensor particles were gently shaken and left for a time period of 24–48 h. In this way, sensor particle sizes separated by their density and can be pipetted from specific depths. For microfluidic test-case, we only sampled sensor particles which stayed dissolved for a time period of 48 h. Similarly, centrifugation was applied to sensor particles in the aggregate test-case. We note that, in addition to this study, the biocompatibility of similar sensor particles was previously tested in different applications for algae, other colony-forming corals and seagrass roots (Koren et al., 2015, 2016; Trampe et al., 2018).

Exciting and measuring sensPIV particles

In order to meet the illumination requirements for sensPIV imaging (≥10 Hz), high light intensities are required. In the past, such requirements were only fulfilled by high-energy continuous-wave or pulsed laser diodes, however, those limit the applicability as the costs are high, special requirements for safe operation are needed and experimental designs can become very complex. These methodological limitations can be overcome with new ultra-bright light emitting diode (LED) systems that can reach light intensities similar to laser diodes. The commercially available LED systems applied in the coral and particle test case have powers ranging between 2.5 W (Wavelength dependent, Omicron, LedHUB, here used for rapid lifetime imaging) and 5 W (LPS3, ILA5150 GmbH, here used for ratiometric imaging). Collimation of LED light is challenging but using state-of-the-art optics, light sheets with widths of 500–1000 μm can be generated (Willert et al., 2010). To achieve this, the LED light was directed via a fiber bundle into the light sheet optics. In front of a cylindrical lens, the fiber bundle was aligned in a linear arrangement resulting in a light-sheet thickness of ~1000 μm (e.g. Figure 1 j). A second cylindrical lens was applied to yield a converging light sheet that minimizes the light sheet to

a thickness of <500 μm over a depth of ~2 mm. In many systems it is important to limit the total light exposure to avoid thermal convection or avoid substantial photosynthetic activity, therefore we triggered the light source via the camera and reduced the recording period to less than 5 s. However, to test if the high excitation light intensity affected the O_2 measurements within the coral test-case, we implanted a microsensor into the tissue where the photosynthetic symbionts are located, and observed an O_2 production of less than 10 μmol L^{-1} within the 2 s recording period with light exposure.

It should be noted that the optimal imaging frequency depends on the system of interest. In some microscale applications, such as the beating of cilia or flagella, recording frequencies of more than 100 Hz have to be achieved. In this case, the response-time of the sensor particles has to be considered. The O_2-dependent quenching of the sensor particles is diffusion limited and, thus, depends on the size of the particles. For the precipitated particles, the median size was 590 ± 360 nm resulting in the diffusion timescale of $\tau = a^2 D^{-1} = 0.4$ ms – 1 ms. This implies that at recording frequencies of below 1000 Hz the sensor particles adapt quasi-instantaneously (compare Video S1). However, as the sensor-particle distribution is relatively wide, up to 5 μm, care has to be taken that the response-time of the sensor particles is not affecting the interpretation of results obtained through high-speed imaging (see also section on the limitations of sensPIV).

The lifetime of the O_2-sensitive dye (~60 μs) can be estimated via repeated imaging of the declining fluorescence intensity after light exposure (see for example (Koren et al., 2019)). This requires shutter-modulated cameras with a temporal resolution of order 10–100 s due to relatively slow sensor readout times and low light intensities employed in most experiments. Recent technical advances, namely a two-tap QMFLIM2 image sensor (pco.FLIM, PCO AG) allows us to estimate the lifetime τ (~60 μs) in the frequency domain based on the frequency-shift, ΔΦ, induced by the quencher (O_2). Applying the camera allows us to keep light-intensities at a high level. Lifetime and frequency-shift are directly related through the equation $\tau = \tan(\Delta\Phi)/(2\pi f_{mod})$, where f_{mod} is the modulation frequency (~5 kHz). This method improves temporal resolution and lifetime images can be recorded in less than 10s (Koren et al., 2019). In order to improve the temporal resolution further, and to meet the requirements for particle velocimetry (recording frequencies above 10 Hz), we adapted the two-tap QMFLIM2 camera chip (pco.FLIM, PCO AG, Germany), which has in each pixel an in-pixel charge swing separating two taps. Each tap records half the period of the excitation signal, which is a sinus function. In reference experiments, the integration windows of the taps were temporally shifted to maximize the difference between the taps at 100% O_2. The normalized difference of the taps will change with the O_2 concentrations and follows the rising flank of the sinus wave which is well represented by a second-order polynomial fit (see also Figure S3). It has to be ensured that the expected quenching through O_2 results in a phase of much less than 90° at the given modulation frequency. Further, the in-pixel swing leads to an asymmetry of the two in-pixel taps that is intensity-dependent. This asymmetry was corrected by recording a homogeneously illuminated object with a wavelength matching the emission wavelength of the O2-sensitive dye. A telecentric lens (TEC – V7X, Computar, USA) was fitted to the camera and a polyester filter (Lee filter, 101 Yellow, Canada) was used to filter the blue excitation light. Sensor particle excitation was achieved through a light sheet using a LedHUB attached to customized light sheet optics (see above).

SensPIV under well-defined O_2 gradients within microfluidic devices

A published microfluidic device design (Rusconi et al., 2014a; 2014b) was adapted to generate known linear O_2 gradients and validate the sensor particle response in heterogeneous conditions. The device consists of two parallel side channels that act as the O_2 source and sink, respectively, and a central channel where the O_2 gradient develops. See the device dimension and channel system cross-section in Figure 2.

The micro-channel system was designed with AutoCAD software (Autodesk, USA) and printed on a plastic photolithography mask (microlitho.co.uk). Then, a silicon wafer was spin coated with SU-8 photoresist (SU-8 2150, Micro-Chem company, US) and baked according to manufacturer recommendations to allow the formation of a cross-link between the photoresist and the silicon substrate. This step was repeated until the desired photoresist thickness (here 750 μm) was achieved. The photolithography mask was placed upon the photoresist-wafer complex in an alignment machine and exposed to UV light. After removing the mask from the photoresist, the whole wafer was submerged in an organic solvent (mr-DEV 600, micro resist technology) to dissolve the portions of the photoresist which were not cross-linked. A master was formed with the polymerized features on the silicon wafer.

The device was fabricated using standard PDMS replica molding procedures. Briefly, a 1:10 vacuum degassed PDMS solution consisting of curing agent: PDMS base (SYLGARD 184 Silicon Elastomer Base, Sigma-Aldrich Co., US) was poured onto the mold and thermally cured for at least 8 h at 80°C. After curing, devices with a thickness of 5 mm were cut using a scalpel and peeled away. The PDMS device was plasma treated for 30 s (Zepto, Diener electronic GmbH, Germany) and bonded onto a 75 × 50 mm microscopy slide (2947–75×50, Corning Inc., US). Inlet and outlet ports were punched using a biopsy punch (Miltex Biopsy Punch, Integra LifeSciences Co., US). The resulting device was placed onto a heating plate set to 80°C for 5 h to improve bonding. Final channel widths and heights were 400 and 750 μm, respectively. The PDMS wall separating the fluidic test channel from the gas channels was 400 μm. The overall length of the serpentine pattern was 532 mm.

PtTFPP sensor particles, produced via the staining method, were calibrated under two O_2 levels within the microfluidic device. Before experiments, the two side channels were connected to two high-precision flow controllers (Cole Parmer, IL) via O_2 impermeable tubing (Masterflex 06404–14, Norprene, Saint-Gobain, France) and a small connecting piece (~10 cm) of Tygon tubing (Tygon, inner diameter 0.5 mm, outer diameter 1.5 mm, Saint-Gobain, France). The inlet of the central channel was connected to a 1 mL gastight syringe (Hamilton #1001, Reno, NV) mounted onto a syringe pump (neMESYS, CETONI GmbH, Germany) in order to control particle flow rates. First, N_2 was supplied into both side channels for 40 min to reach 0% air saturation within the gas permeable

PDMS device. After this equilibration period, a solution of sensPIV particles was introduced into the central channel filled with MQ water and thereafter the flow was stopped to keep particles still. Particles in the main channel were then equilibrated to 0% air saturation for 20 min and imaged using an inverted Nikon Ti-E microscope (Nikon inc., Tokyo, Japan) and an sCMOS camera (Andor Zyla 4.2, Oxford instruments, Belfast, UK); first by phase contrast using an LED white-light illuminator and then in fluorescence by excitation at 392 nm (Spectra X light engine, Lumencor Inc., Beaverton, OR, US). This was repeated for several locations along the central channel to obtain the calibration of particles for 0% O_2. To calibrate particles at 100% air saturation, compressed air was supplied to both side channels and the above calibration procedure was repeated again. In order to identify particles and relate the O_2 concentration to their fluorescence intensity, we applied a particle boundary tracing algorithm. First, brightfield images were pre-processed by tuning brightness, contrast and background subtraction. Then particles were identified through intensity thresholding and only particles with a circularity larger than 0.7 were included in the post-processing.

Experiments in microfluidic devices were performed with sensPIV particles under flow as well as no-flow conditions. In order to study the evolution of dissolved-O_2 over time, we simulated the dissolved-O_2 transport inside the microfluidic chips using a multiphysics COMSOL model based on the 3D microfluidic channel geometry. The flow field was simulated by solving the Stokes equations:

$$0 = -\nabla p + \mu \nabla^2 u \quad \text{(Equation 2)}$$

where u is the velocity vector, p the pressure, μ dynamic viscosity and ∇ the gradient operator. The continuity equation for incompressible fluids reads:

$$\nabla \cdot u = 0 \quad \text{(Equation 3)}$$

The O_2 distribution in the microfluidic chip was then calculated solving the advection-diffusion equation:

$$\frac{\partial C}{\partial t} = D\nabla^2 C - u \cdot \nabla C \quad \text{(Equation 4)}$$

where D is the diffusion coefficient for O_2 in PDMS and water ($D_{O2,PDMS} = 3.25 \times 10^{-9}\ m^2\ s^{-1}$, $D_{O2,water} = 2.01 \times 10^{-9}\ m^2\ s^{-1}$ based on a temperature of T = 293.15 K (Markov et al., 2014)) and C is the O_2 concentration. For all walls we assumed no-slip boundary conditions. The flow field was driven by the prescribed flow rate set by the syringe pump. To achieve a realistic O_2 distribution, the gas concentration of the outer channels was imposed at the boundary and saturated O_2 concentrations at the inlet were assumed.

Measuring the dynamic O_2 exchange around a model laboratory aggregate

Model laboratory aggregates were prepared by mixing 2.48 mg mL^{-1} of sensor particles (produced via the precipitation method) with 0.7% agarose (Biozym, Germany). Agarose was dissolved in Milli-Q (MQ) water by boiling the mixture in a microwave. Subsequently, the solution was cooled down to ~40°C and sensPIV particles were added and thoroughly mixed. In order to form spherical particles the prepared agarose solution was pipetted into a glass beaker containing MQ water overlaid with cold canola oil (Ja! Canola Oil, Rewe). While cooling, the oil induced the formation of spherical model particles that subsequently sank from the oil layer into the MQ water. Particles were filtered using a 100 μm plankton mesh (Hydro-Bios, Germany), washed in MQ water and stored in the dark.

Experiments with model aggregates were performed in a recirculating glass flow chamber (height: 10.7 cm; diameter: 2.5 cm). To provide a homogeneous flow field, the glass chamber was connected via a 3D-printed polyether ether ketone (PEEK, FKM Sintertechnik Gmbh, Germany) inlet which had 1 mm capillaries, to a gear pump (ISMATEC, ISM901B, Germany). The pump volume was adjusted to achieve a flow velocity of 2.1 mm s^{-1} inside the flow chamber. The entire chamber was immersed in an aquarium filled with MQ water (dimensions: 18.4 × 9.7 × 9.7 cm) to stabilize the temperature at 20°C. Prior to all experiments, the particle was degassed overnight using N_2 gas and only then attached to a needle connected to a motorized linear drive (Faulhaber, T-LSR75A, Germany). This allowed for the precise positioning of the agarose particle into the center of the recirculating glass flow chamber.

Calibration of the sensor particles was performed in the flow chamber via a degassing setup at ten different O_2 concentrations under the same conditions as in the experiments. The target O_2 concentrations were cross-checked with a microsensor (OXR430, Pyroscience, Germany). The O_2 concentration was reconstructed by decomposing the field of view into the interior of the aggregate and the outside of the aggregate. Care had to be taken to ensure that the darker image I_{T2} did not fall below the noise level, in which case the normalized intensity would not be uniquely associated with a specific O_2 concentration. In case I_{T2} fell below the noise level we performed calibration based on the difference of I_{T2} and I_{T1} which yielded good results. Flow fields were determined using a kinematic prediction algorithm (https://web.stanford.edu/~nto/LPT.shtml, Last Visit: 8/9/2021) in Matlab (2018b, Mathworks). In each image, 1154 ± 23 sensor particles were tracked and the reconstructed PTV tracks ranged between 5 and 463 individual data points.

SensPIV for the visualization of O_2 dynamics and vortical flows around the coral *P. lutea*

We adapted a custom-built light sheet microscopy recirculating flow chamber setup (see (Pacherres et al., 2020) for details, schematic in Figure 4) with which we performed ratiometric O_2 measurements, PIV and PTV around a live coral specimen. A small fragment of the coral *P. lutea,* roughly 2 cm in size, was placed into the flow chamber and a free-flow velocity of 1500 μm s^{-1} was imposed. After an equilibration period of 10 min, 1 mL of sensPIV particle stock solution (1 mg mL^{-1}) was added to the flow-chamber resulting in a final concentration of 0.025 mg mL^{-1}. In order to minimize mucus production, the coral was only exposed for short time

periods (<2 min) to sensor particles before filtering away the remaining particles via a syringe filter (0.22 μm, Millex) placed into the recirculation system. All experiments were performed in a temperature controlled room at 25 °C. The sensor particles were illuminated with a blue LED (450 nm ± 30nm, LPS3, ILA GmbH, Germany) using light sheet optics (see also Figure 4A). Imaging was performed using an RGB camera (Grasshopper3, SONY ICX625, FLIR) through a custom-built microscopic lens array (based on Qioptiq Optem-Fusion System, Germany). Exposure times were reduced to below 20 ms and the light was triggered by the camera to minimize light exposure to the coral. The blue channel was used to determine the surface of the coral using an in-house developed tracking algorithm. PIV was performed based on the red channel (Em. > 550 nm) of the camera chip using standard cross-correlation techniques of two subsequent images using the software PIVView (Pivtec GmbH, Germany, see also Figure S2), and PTV was performed based on a kinematic prediction algorithm (https://web.stanford.edu/~nto/LPT.shtml, Last Visit: 8/9/2021) in MATLAB (2018b, Mathworks). For both techniques, the images were pre-processed with a five px kernel Gaussian high-pass filter to remove the background noise and signals of smaller particles. For PIV, we applied a multi-grid refinement technique with an initial window size of 256 px (approx. 460 μm for the coral test-case) and final window size of 64 px (approx. 115 μm). The window sizes were adjusted to achieve a sufficient particle density (7-9 particles) of larger sensor particles in each interrogation window. Depending on the flow features, it may be desirable to increase the particle density which can be achieved by increasing sensor-particle concentrations which will not affect calibration (compare Figure 1G). O_2 concentrations were determined based on ratiometric measurements of the red and green channel: $I_R = R/G$ after calibration at various O_2 concentrations using Equation (1). All image post-processing was performed in MATLAB (2018b, Mathworks). The boundary layer thickness was determined based on the average location where O_2 decreases to 10% of the surface concentration (compare also Figure S5).

It should be noted that during the calibration procedure, we observed an emission of schott-glass filters that can affect the ratiometric measurements and corrections would require an additional light-dependent referencing of the applied filter. However, the problem can be overcome by using polyester filters (e.g. Lee filters, Canada). In addition to the sensPIV measurements, an electrochemical microsensor with a tip size of 20 μm (Unisense, Denmark) was used for comparison and to cross-reference the measurements. The microsensor was attached to an XYZ-micromanipulator (Unisense, Denmark) to perform profiles for comparison. O_2 measurements were performed in 20 μm steps.

QUANTIFICATION AND STATISTICAL ANALYSIS

Details of the statistical methods used in this study, such as the averaging procedure for improving signals of sensor particles, are described in detail in the respective sections and in the supplemental information that is available below. The number of replications for the measured parameters are described along with the presented means, or/and presented as distributions if sample size was sufficient. For linear regressions the fitting parameters along with statistical measures are present in the main text or in the supplemental information. Experimental results are cross-compared with numerical models or other methods such as O_2-microsensor measurements.